

# Finite Element-Based Failure Models for Carbon/Epoxy Tape Composites

A Master Thesis  
Presented to  
The Academic Faculty  
by

Guillaume Seon

In Partial Fulfillment  
of the Requirements for the Degree  
Master of Science in Aerospace Engineering

Daniel Guggenheim School of Aerospace Engineering  
Georgia Institute of Technology  
May 2009  
Copyright © 2009 by Guillaume Seon

# Finite Element-Based Failure Models for Carbon/Epoxy Tape Composites

Approved by:

Dr. Andrew Makeev, Advisor

Daniel Guggenheim School of Aerospace Engineering  
*Georgia Institute of Technology*

Dr. Olivier Bauchau

Daniel Guggenheim School of Aerospace Engineering  
*Georgia Institute of Technology*

Dr. Erian Armanios

Daniel Guggenheim School of Aerospace Engineering  
*Georgia Institute of Technology*

Date Approved: March 16, 2009

# ACKNOWLEDGEMENTS

I would like first to express my greatest gratitude to my advisor, Dr. Andrew Makeev, who inspired me to step into composite material failure mechanisms. His supervision, advice and guidance as well as his wide experience in composite science and scientist intuition are the backbone of this work. His enthusiasm and competence nourished my wish to work in the field of composite materials in the aerospace industry.

I would also like to deeply thank senior research engineer Dr. Yuri Nikishkov for all his generous assistance and especially for kindly sharing his finite elements models with me. His critical comments on my work, discussions and his knowledge in computational coding have been extremely helpful for this study.

I thank the committee members Dr. Olivier Bauchau and Dr. Erian Armanios for reading this thesis and for their comments and suggestions.

I wish to thank Ph.D. student Yihong He who helped me to get introduced to finite element software ABAQUS in the early stages of this work.

I would like to express my gratitude to all my friends that shared with me this experience as a graduate student in the United States, for all the support, the comradeship and caring they provided.

Lastly I wish to thank my parents for their encouragement and education they gave me and made that work and experience abroad possible.

# TABLE OF CONTENTS

ACKNOWLEDGEMENTS.....	iii
LIST OF TABLES .....	vi
LIST OF FIGURES.....	vii
SUMMARY .....	x
CHAPTER 1: INTRODUCTION .....	1
CHAPTER 2: Failure prediction for carbon/epoxy Tape Laminates with Wavy Plies .....	3
2.1    Problem Presentation .....	3
2.2    Material Characterization.....	7
2.2.1    Linear properties .....	7
2.2.2    Nonlinear Interlaminar Shear Stress-Strain Relations.....	13
2.3    Finite Element Analysis for Large Wrinkle Coupons .....	16
2.3.1    ABAQUS Finite Element Model.....	16
2.3.1.1    Plane Stress Mesh .....	16
2.3.1.2    Non-linear Interlaminar Shear Properties .....	18
2.3.1.3    Local Material Orientation.....	20
2.3.2    Finite Element Predictions.....	21
2.3.3    Test Data Comparison.....	25
2.4    Finite Element Analysis for Small Wrinkle Coupons .....	35
2.4.1    ABAQUS Finite Element Model.....	35
2.4.2    Finite Element Predictions.....	36
2.4.3    Test Data Comparison.....	38
2.4.4    Suggestions to Assess the Porosity Problem .....	44
2.4.4.1    Modifying the Geometry .....	44
2.4.4.2    Modifying the Material Strength.....	47

CHAPTER 3: Failure Prediction for Open Hole Carbon/epoxy Laminate .....	49
3.1    Problem Presentation .....	49
3.2    ABAQUS Finite Element Model .....	50
3.2.1    3D Finite Element Mesh .....	50
3.2.2    Mesh Convergence .....	52
3.2.3    Failure Model .....	58
3.2.3.1 <i>Damage Initiation Criterion</i> .....	58
3.2.3.2 <i>Damage Propagation</i> .....	60
3.3    Finite Element Analysis Results and Test Comparison .....	61
3.3.1    Fiber Oriented Finite Element Mesh .....	61
3.3.2    Finite Element Analysis Results and Test Data Comparison .....	64
3.3.2.1 <i>Matrix Cracking Initiation and Propagation</i> .....	64
3.3.2.2 <i>Test Data Correlation</i> .....	66
CHAPTER 4: CONCLUSION.....	70
REFERENCES.....	72

# LIST OF TABLES

Table 1.	Cross-Section Dimensions and Loads at Matrix Cracking for Ply-Termination Coupons .....	8
Table 2.	Maximum Tensile Strain before Matrix Failure .....	10
Table 3.	IM7/8552 Tape Stiffness Data [10].....	10
Table 4.	IM7/8552 Tape Stiffness and Strength Properties .....	13
Table 5.	Interlaminar Shear Strength and Stiffness Values .....	16
Table 6.	Failure Load Predictions for IM7/8552 Tape Wrinkle Coupons.....	22
Table 7.	Cross-Section Dimensions and Failure Loads for Large-Wrinkle Coupons...	25
Table 8.	Summary of Predictions and Test Data for Wrinkle Coupons .....	34
Table 9.	Failure Load Predictions for IM7/8552 Tape Small Wrinkle Coupons.....	36
Table 10.	Test Data and FEM Predictions for Maximum Strains.....	42
Table 11.	Predicted and Tested Failure Loads for Small Wrinkle Coupons .....	43
Table 12.	Influence of Parameter b in Mesh Convergence for Maximum Stresses ...	53
Table 13.	Dependencies on Damage Field Variables for Matrix Cracking .....	61
Table 14.	Summary of Predictions and Test Data for Hole Coupon.....	68

# LIST OF FIGURES

Figure 1.	IM7/8552 Carbon/Epoxy Tape Large-Wrinkle Coupons .....	4
Figure 2.	IM7/8552 Carbon/Epoxy Tape Small-Wrinkle Coupons .....	5
Figure 3.	Presence of porosity for small-wrinkle coupon C1.....	6
Figure 4.	IM7/8552 Carbon/Epoxy Tape Ply-Termination Coupon A2 .....	7
Figure 5.	Lagrange Strain Contour Plots for Coupon A2 at 892 lbs Tension .....	9
Figure 6.	Lagrange Strain Contour Plots for Coupon A2 at 1031 lbs Tension .....	9
Figure 7.	Measured and Calculated Loads for Coupon A2 .....	12
Figure 8.	IM7/8552 Carbon/Epoxy Tape SBS Test Coupon .....	14
Figure 9.	IM7/8552 Carbon/Epoxy SBS Coupon Failure .....	14
Figure 10.	Shear Stress-Strain Response for Unidirectional IM7/8552 Tape Specimens .....	15
Figure 11.	ABAQUS Sketch for Coupon B2 Geometry .....	17
Figure 12.	Plane Stress Finite Element Mesh for B2 Wrinkle Coupon .....	17
Figure 13.	Convergence of USDFLD non-linear shear stress-strain algorithm.....	19
Figure 14.	Element Based local Coordinate System.....	20
Figure 15.	User Defined Orientation Systems at The Main Wrinkle for B2 FEM .....	21
Figure 16.	Hashin Criterion Contour Plot for Coupon B1 at 3682lbs Tension .....	23
Figure 17.	Hashin Criterion Contour Plot for Coupon B2 at 3360lbs Tension .....	23
Figure 18.	Hashin Criterion Contour Plot for Coupon B3 at 3905lbs Tension .....	23
Figure 19.	ITS Criterion Contour Plot for Coupon B1 at 4296lbs Tension .....	24
Figure 20.	ITS Criterion Contour Plot for Coupon B2 at 3763lbs Tension .....	24
Figure 21.	ITS Criterion Contour Plot for Coupon B3 at 4223lbs Tension .....	24
Figure 22.	Interlaminar Strain Contour Plots for Coupon B1 at 4227 lbs Tension .....	27

Figure 23.	Interlaminar Strain Contour Plots for Coupon B2 at 3544 lbs Tension .....	28
Figure 24.	Interlaminar Strain Contour Plots for Coupon B3 at 4097lbs Tension .....	29
Figure 25.	Lagrange Strain Contour Plots for Coupon B1 at 4227 lbs Tension .....	30
Figure 26.	Lagrange Strain Contour Plots for Coupon B1 at 4248 lbs Tension .....	31
Figure 27.	Lagrange Strain Contour Plots for Coupon B2 at 3544 lbs Tension .....	31
Figure 28.	Lagrange Strain Contour Plots for Coupon B2 at 3550 lbs Tension .....	32
Figure 29.	Lagrange Strain Contour Plots for Coupon B3 at 4097 lbs Tension .....	32
Figure 30.	Lagrange Strain Contour Plots for Coupon B3 at 4101 lbs Tension .....	33
Figure 31.	Plane Stress Finite Element Mesh for Coupon C1 .....	35
Figure 32.	Hashin and ITS Contour Plots for Coupon C1 at Predicted Failure Loads	37
Figure 33.	Hashin and ITS Contour Plots for Coupon C2 at Predicted Failure Loads	37
Figure 34.	Hashin and ITS Contour Plots for Coupon C3 at Predicted Failure Loads	37
Figure 35.	Strain Contour Plots for Coupon C1 at 3086lbs Tension.....	39
Figure 36.	Strain Contour Plots for Coupon C2 at 3129lbs Tension.....	40
Figure 37.	Strain Contour Plots for Coupon C3 at 3156lbs Tension.....	41
Figure 38.	High Strain Concentration Due to Porosity Void for Coupon C1 .....	43
Figure 39.	Global and Submodel Mesh Details for Geometry Enclosed Void. ....	45
Figure 40.	Interlaminar Tensile Strain for C1 at 3156lbs Tension with Rectangular Cavity.....	46
Figure 41.	Subsurface (X-Ray) and Surface (DIC) Images just before Ultimate Failure .....	50
Figure 42.	Global and Sub-model 3D Finite Element Model for Open Hole Coupon ..	51
Figure 43.	Mesh Seed Parameters for Mesh Convergence Study .....	52
Figure 44.	Stresses Plotting Path for Mesh Convergence Study .....	53
Figure 45.	Influence of Circumferential Parameter a for $S_{22}$ Convergence .....	54
Figure 46.	Influence of Radial Parameter c for $S_{22}$ Convergence.....	54



Figure 47.	Influence of Through-thickness Parameter $t$ for $S_{22}$ Convergence.....	55
Figure 48.	Influence of Circumferential Parameter $a$ for $S_{12}$ Convergence .....	55
Figure 49.	Influence of Radial Parameter $c$ for $S_{12}$ Convergence.....	55
Figure 50.	Influence of Through-thickness Parameter $t$ for $S_{12}$ Convergence.....	56
Figure 51.	Influence of Circumferential Parameter $a$ for $S_{33}$ Convergence.....	56
Figure 52.	Influence of Radial Parameter $c$ for $S_{33}$ Convergence.....	56
Figure 53.	Influence of Through-thickness Parameter $t$ for $S_{33}$ Convergence .....	57
Figure 54.	Damage Contour plot at 6240lbs for 90 deg surface ply .....	62
Figure 55.	Global and Sub-model Meshes for Open Hole Coupon Analysis .....	63
Figure 56.	Damage Plot for Open-Hole Coupon at 4226 lbs Tension .....	64
Figure 57.	Damage Plot for Open-Hole Coupon at 4991 lbs Tension .....	64
Figure 58.	Damage Plot for Open Hole Coupon at 5953 lbs Tension .....	65
Figure 59.	Damage Plot for Open Hole Coupon at 8475 lbs Tension .....	65
Figure 60.	Ultimate Failure Crack for Open Hole Coupon.....	66
Figure 61.	Surface Transverse Strain Correlation at 1st 45 deg. Crack Development .. .....	67
Figure 62.	Surface Shear Strain Correlation at 1st 45 deg. Crack Development.....	67
Figure 63.	Surface Transverse Strain Correlation at Ultimate Crack Development....	67
Figure 64.	Surface Shear Strain Correlation at Ultimate Crack Development .....	68

# SUMMARY

Laminated carbon/epoxy composite structures are increasingly used in the aerospace industries. Low weight, elastic tailoring, and high durability make the composite materials well suited for replacement of conventional metallic structures. However the difficulty to capture structural failure phenomena is a significant barrier to more extensive use of laminated composites.

Predictions are challenging because matrix (resin) dominated failure mechanisms such as delaminations and matrix cracking contribute to the structural failure in addition to fiber-dominated failures. A key to rigorous failure predictions for composites is availability of measurements to quantify structural model parameters including matrix-dominated stress-strain relations and failure criteria. Novel techniques for measurement of nonlinear interlaminar constitutive properties in tape composites have been recently developed at Georgia Institute of Technology. Development of methods for accurate predictions of failure in carbon/epoxy tape laminate configurations with complex lay-ups is the main focus of this work. Failures through delamination and matrix cracking are considered.

The first objective of this effort is to implement nonlinear interlaminar shear stress-strain relations for IM7/8552 carbon/epoxy tape in ABAQUS finite element models and validate structural delamination failure predictions with tests. Test data for composite configurations with wavy fibers confirm that nonlinear interlaminar shear stress-strain response enables accurate failure prediction. The problem of the presence of porosity and its influence on failure was noted. The second objective is to assess the ability to simulate initiation and propagation of matrix-ply cracking. Failure models for IM7/8552 carbon/epoxy tape open-hole tensile coupons are built and validated.

# CHAPTER 1: INTRODUCTION

Laminated carbon/epoxy composite structures are increasingly used in the aerospace industries. Low weight, elastic tailoring, and high durability make the composite materials well suited for replacement of conventional metallic structures. However anisotropy and non-linear stress-strain response as well as complexity of the failure processes contribute to the complexity of their structural behavior. One of the most significant barriers to more extensive use of laminate composite materials is the difficulty to capture structural failure phenomena. Predictions are challenging because matrix (resin) dominated failure mechanisms such as delaminations and matrix cracking contribute to the structural failure in addition to fiber-dominated failures.

A key to rigorous failure predictions for composites is availability of measurements to quantify structural model parameters including matrix-dominated stress-strain relations and failure criteria. Accurate transverse (through-the-thickness) constitutive properties are especially important for structural analysis of thick composites. Examples of thick composite applications include rotor blade spar and blade-to-hub attachment structural details of rotary wing aircraft [1]. Carbon/epoxy materials such as IM7/8552 tape are oftentimes used for such structures.

The problem of structural failure predictions in carbon/epoxy composites has received a lot of attention from researchers over the past years. Finite element-based techniques such as cohesive zone models have been developed to address the matrix-dominated failure phenomena including delaminations and ply-cracks [2]. Researchers also worked on the definition of accurate failure criteria taking into consideration combined effects of different failure modes and fracture-corrected strength properties [3]. Good correlation

between predictions and experimental results has been demonstrated for simple (not practical) laminate configurations with small number of plies [2].

Development of methods for accurate predictions of failure in carbon/epoxy tape laminate configurations with complex lay-ups is the main focus of this work. Non-linear interlaminar constitutive properties are required for accurate failure predictions of thick composites [4]. In this work the non-linear interlaminar constitutive properties are included in finite element-based models and failure criteria.

Novel techniques for measurement of nonlinear interlaminar constitutive properties in composites have been recently developed at Georgia Institute of Technology [4]. The first objective of this effort is to implement the nonlinear interlaminar shear stress-strain relations obtained from tests data for IM7/8552 carbon/epoxy tape in ABAQUS finite element models and validate structural delamination failure predictions with tests. Delamination of composite configurations with wavy fibers will be considered. The problem of the presence of porosity and its influence on failure was noted.

The second objective is to assess the ability to simulate initiation and propagation of matrix-ply cracking. Failure models for IM7/8552 carbon/epoxy tape open-hole tensile coupons are built and validated.

## **CHAPTER 2: Failure prediction for carbon/epoxy Tape Laminates with Wavy Plies**

### **2.1 Problem Presentation**

Fiber waviness is a manufacturing defect oftentimes present in thick composites including rotorcraft parts [5]. It can be the result of uneven curing pressure, resin shrinkage or ply-buckling prior to curing. This defect can create significant degradation of material structural properties such as degradation of tensile and compressive strength and fatigue life. Carbon/Epoxy tape laminates with wavy plies defects under tensile loads will be considered. Failure through delamination that initiates at wrinkles locations is expected to occur because of high interlaminar tensile and shear stresses. This study has for objectives to verify the accuracy of the interlaminar failure models for delamination.

Two types of laminate were selected with different sizes of wrinkles. For the first set of coupons, carbon/epoxy laminates with higher radius of curvature wrinkles were manufactured. A 88-ply  $[(+45_3/0_2)_3/(\pm 45_4/0_2)/(\pm 45_4/0_4/\pm 45_4)/(0_2/\pm 45_4)/(0_2/\pm 45_3)_3]_T$  lay-up of material IM7/8552 is selected. Three 0.14-inches-wide tensile coupons (B1, B2, and B3) were machined from a single 0.64-inches-thick panel. The coupon length is 6 inches and a gage (untabbed) length is 2.95 inches. Figure 1 shows the wavy (wrinkle) regions in the coupons.

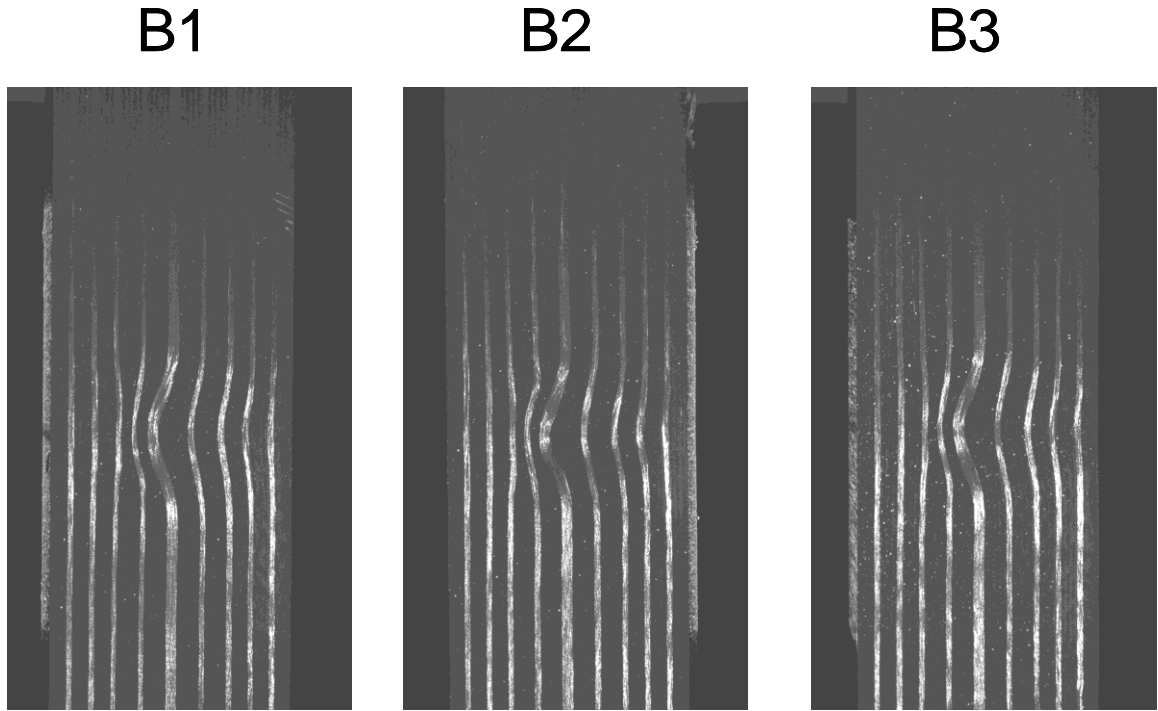


Figure 1. IM7/8552 Carbon/Epoxy Tape Large-Wrinkle Coupons

Specimen B2 is expected to fail at a lower load compared to B1 and B3 as the main wrinkle in the specimen B2 has a higher height-to-length aspect ratio.

The second set of coupons consists in laminates with smaller height-to-length aspect ratio wrinkles. Same material IM7/8552 is selected with a slightly different 104-ply  $[(+45_6/0_4)_3/(+45_8/0_4)/(+45_8/0_4/+45_8)/(0_4/+45_8)/(0_4/+45_6)_3]_T$  lay-up machined from a 0.75-inches-thick panel. Gage length is 3 inches. Figure 2 shows small-wrinkle coupons.

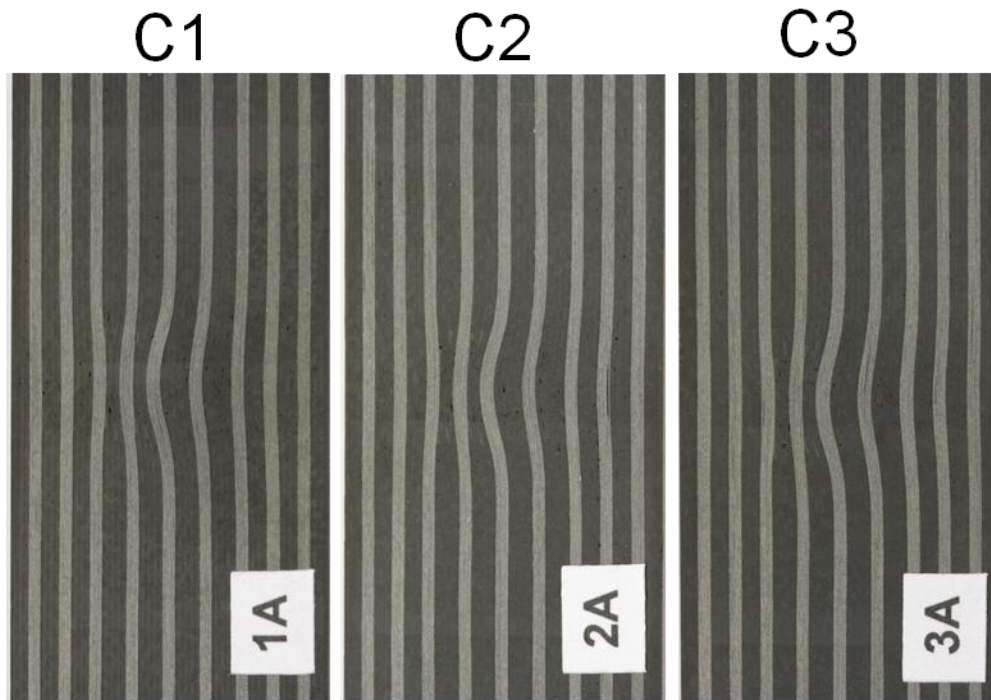


Figure 2. IM7/8552 Carbon/Epoxy Tape Small-Wrinkle Coupons

Small-wrinkle specimens are expected to fail at higher loads compared to large wrinkle coupons, due to the fact that they are thicker and that lower wrinkles' height-to-length aspect ratios result into lower stress concentrations.

However it is worth noting that a closer inspection of the specimens reveals a widespread presence of porosity defects for the small-wrinkle coupons. Porosity is a common defect in thick carbon/epoxy tape composites [6]. It includes microscopic interfacial voids in the matrix material located between the plies and scattered throughout the thickness. This defect occurs primarily because of air bubbles and volatile substances liberated during curing. Porosity is the consequence of many factors difficult to control, but in many cases, insufficient pressure during curing is the primary factor of its formation. Porosity is hard to detect from the surface since it occurs inside

the material; nevertheless, nondestructive ultrasonic-based detection methods [7] have been developed in the aerospace industry during the past years.

In the present work, the wrinkle coupons were cut through the thickness of a single composite panel and voids are visible on both sides of the coupons. Figure 3 illustrates the presence of porosity for coupon C1.

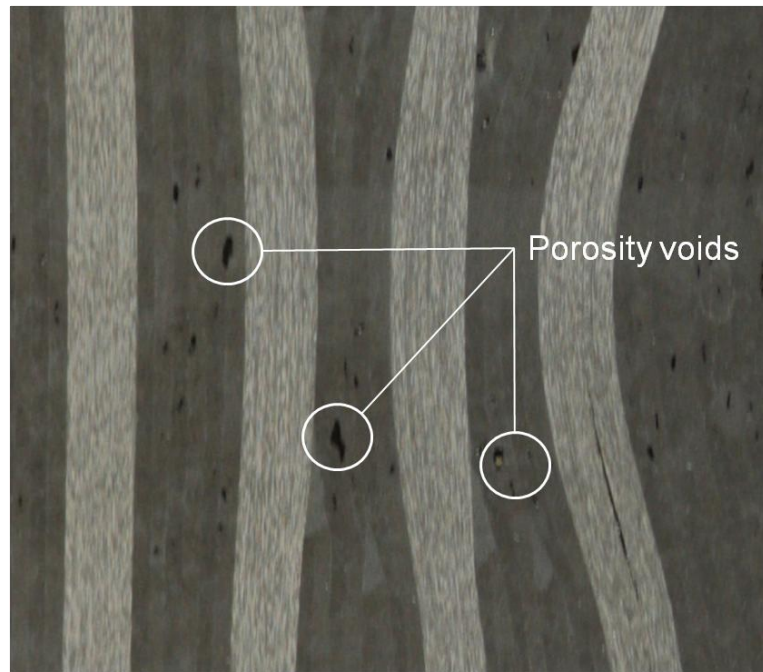


Figure 3. Presence of porosity for small-wrinkle coupon C1

Such manufacturing defects are not present in the large wrinkle coupons B1, B2 and B3, subject to higher curing pressure. Large-wrinkle and small-wrinkle coupons were manufactured with different curing pressure, which explains that difference. Significantly higher pressure was applied to generate the large wrinkles and these specimens are free of visible porosity defects.

The study of small wrinkle coupons will include the assessment of porosity's influence on the quality of failure predictions.



## 2.2 Material Characterization

### 2.2.1 Linear properties

Before building finite element models of the considered composite tapes, available material constitutive properties for IM7/8552 tape were verified and completed using test data from three ply-termination tensile coupons A1, A2, and A3 under tensile load.

Coupons are waviness-free and porosity-free and a 88-ply lay-up is oriented according to the following stacking sequence:

$[(\pm 45_3/0_2)_3/(\pm 45_4/0_2)/(\pm 45_4/0_4/\pm 45_4)/(0_2/\pm 45_4)/(0_2/\pm 45_3)_3]_T$ . The ply-termination coupons are 6 inches-long (untapped length 2.95 in.), 0.64 inches-thick and 0.13 inches-wide.

Figure 4 shows the ply-termination areas for one of the coupons (A2).

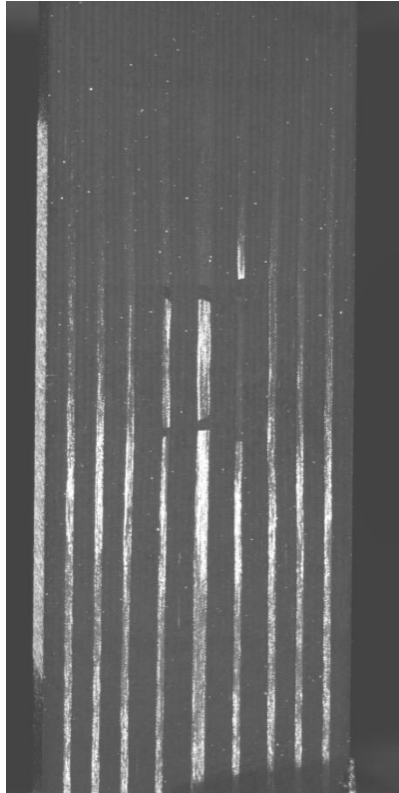


Figure 4. IM7/8552 Carbon/Epoxy Tape Ply-Termination Coupon A2

Three adjacent zero-degree ply-groups are cut at two locations to introduce the ply-terminations. As prepreg is cut before curing, resin fills the ply-termination areas in the cured coupons. Table 1 lists the cross-section dimensions and loads at matrix cracking onset.

Table 1. Cross-Section Dimensions and Loads at Matrix Cracking for Ply-Termination Coupons

Test Specimen	W (in)	T (in)	Load (lbs)
A1	0.6385	0.1258	808 to 953
A2	0.6393	0.1256	892 to 1031
A3	0.6398	0.1253	901 to 1050

A Digital Image Correlations (DIC) full-field strain measurement technique was used for monitoring surface strains. The DIC strain measurement is based on quantifying locations of a random texture on specimen surface [8] to measure surface shape and deformation. The random texture is generated using white and black spray-paints. A stereo digital camera set (white-light optics, no laser) is used to measure 3D surface shape and deformation. A commercially available DIC tool VIC-3D [9] is utilized.

Figure 5 shows contour plots for Lagrange strain tensor components for coupon A2 at 892 lbs tensile load, and Figure 6 shows the strain contour plots at 1031 lbs tensile load at which the first matrix crack was detected.

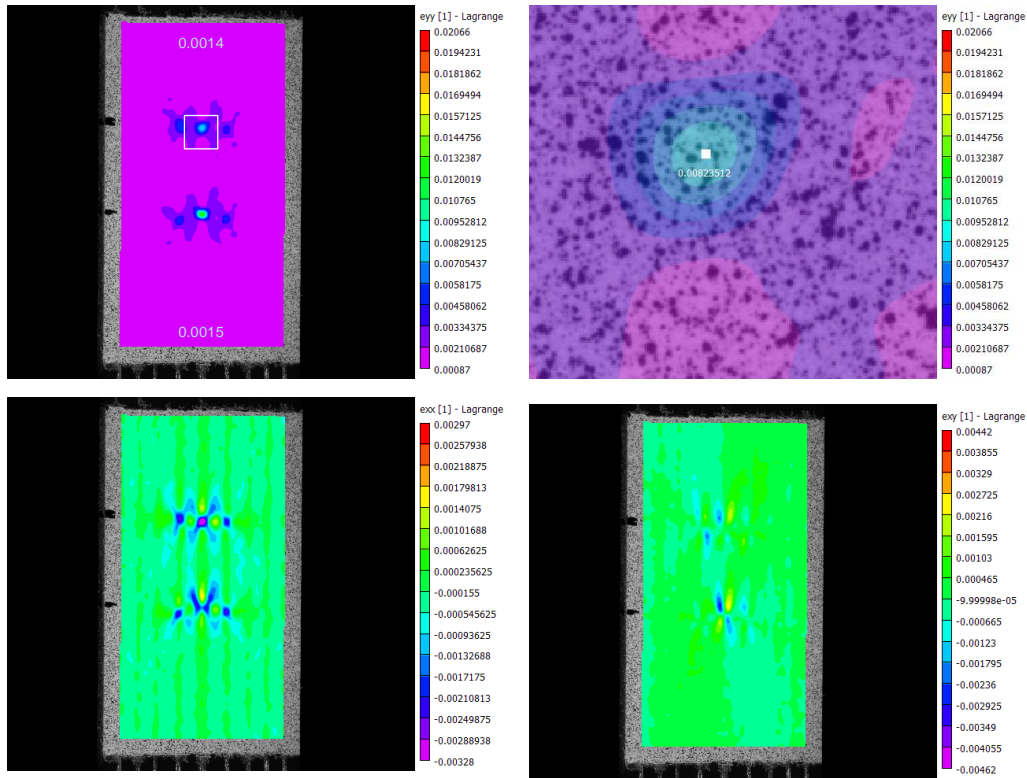


Figure 5. Lagrange Strain Contour Plots for Coupon A2 at 892 lbs Tension

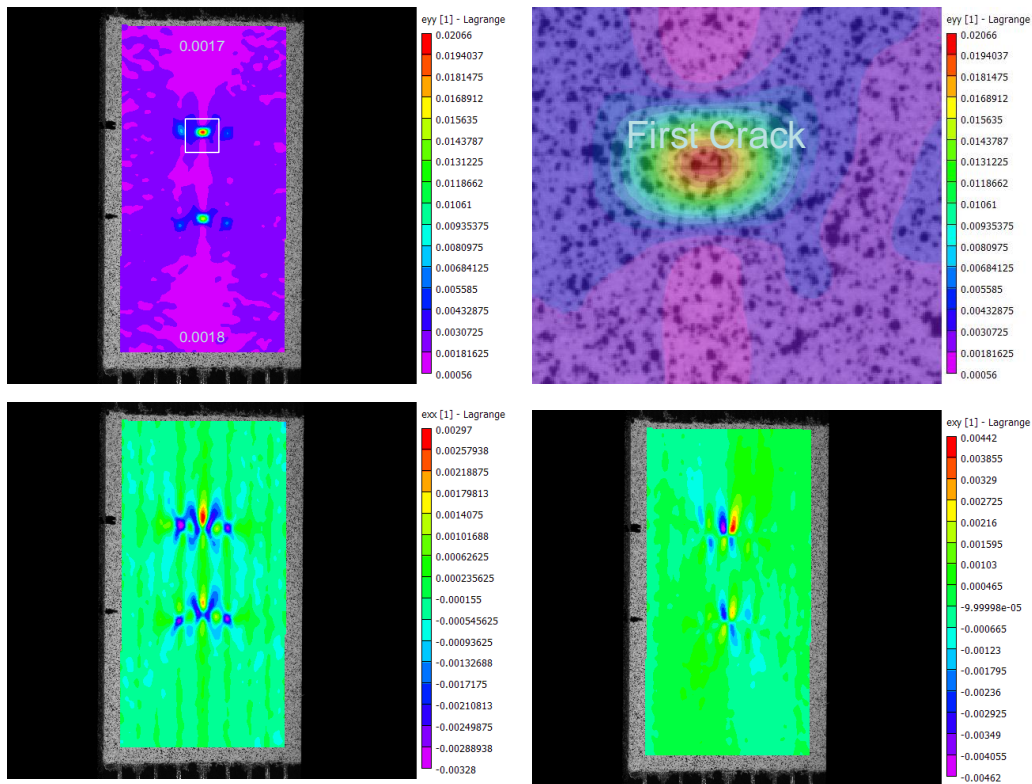


Figure 6. Lagrange Strain Contour Plots for Coupon A2 at 1031 lbs Tension

The coordinates  $x$  and  $y$  correspond to the coupon transverse and axial directions, respectively, and  $\epsilon_{xy} = \gamma_{xy}/2$  is the tensor shear strain. The maximum tensile strain value in the resin before cracking is indicated with a point. The random texture is also depicted in the Figures. Table 2 lists the maximum tensile strain values before matrix cracking (the average value is also listed).

Table 2. Maximum Tensile Strain before Matrix Failure

Test Specimen	Load (lbs)	Maximum Tensile Strain ( $\mu\epsilon$ )
A1	808	8524
A2	892	8235
A3	901	8874
AVG	867	8544

A 8544  $\mu\epsilon$  tensile strain is used as a strain-based matrix failure criterion.

Table 3 lists stiffness data for IM7/9552 Tape available in open literature [10].

Table 3. IM7/8552 Tape Stiffness Data [10]

Tensile Moduli (msi)	
$E_{11}$	24.8
$E_{22}$	1.3
Shear Modulus $G_{12}$ (msi)	0.77
Poisson's Ratio $\nu_{12}$	0.32

Although no published three-dimensional constitutive properties are available for thick IM7/8552 Carbon/Epoxy tape configurations, Dr. Andrew Makeev previously conducted a 3D assessment for IM7/5250-4 Carbon/BMI tape which exhibits similar stiffness properties to IM7/8552 tape at room temperature. ASTM Standard tensile and V-notch

shear test coupons [12],[14] as well as torsion test coupons were machined from a 0.75-inch-thick panel to generate tensile modulus  $E_{11}$  and  $E_{22}$ , Poisson's ratio  $\nu_{13}$  and  $\nu_{23}$ , and shear modulus  $G_{13}$  and  $G_{23}$  properties. ASTM Standard tensile and in-plane shear modulus data [12],[13] were also generated for thin laminates. The following observations were made: The average RT tensile modulus  $E_{11}$  value for the thick coupons was 10% lower compared to the thin coupons; Poisson's ratio  $\nu_{23}$  value was 0.5; and transverse isotropic constitutive response including  $G_{23} = E_{22}/2/(1 + \nu_{23})$  was measured. Such results were used in this work to assume 3D stiffness properties for IM7/8552 tape.

To verify material stiffness data for finite element models of the wrinkle coupons, DIC strain data for ply-termination coupons and linear elasticity assumptions [11] were utilized. The average ply strains far from the ply-termination locations were converted to axial force components for each ply group. Transverse isotropy and  $\nu_{23} = 0.5$  were assumed to calculate the out-of-plane properties:  $E_{33} = 1.3$  msi,  $G_{13} = 0.77$  msi, and  $G_{23} = 0.43$  msi. The axial modulus  $E_{11}$  was varied to match load measurements. Measured and calculated loads match for  $E_{11} = 22.3$  msi which is a 10% modulus reduction. Figure 7 shows loads correlation for the A2 coupon.

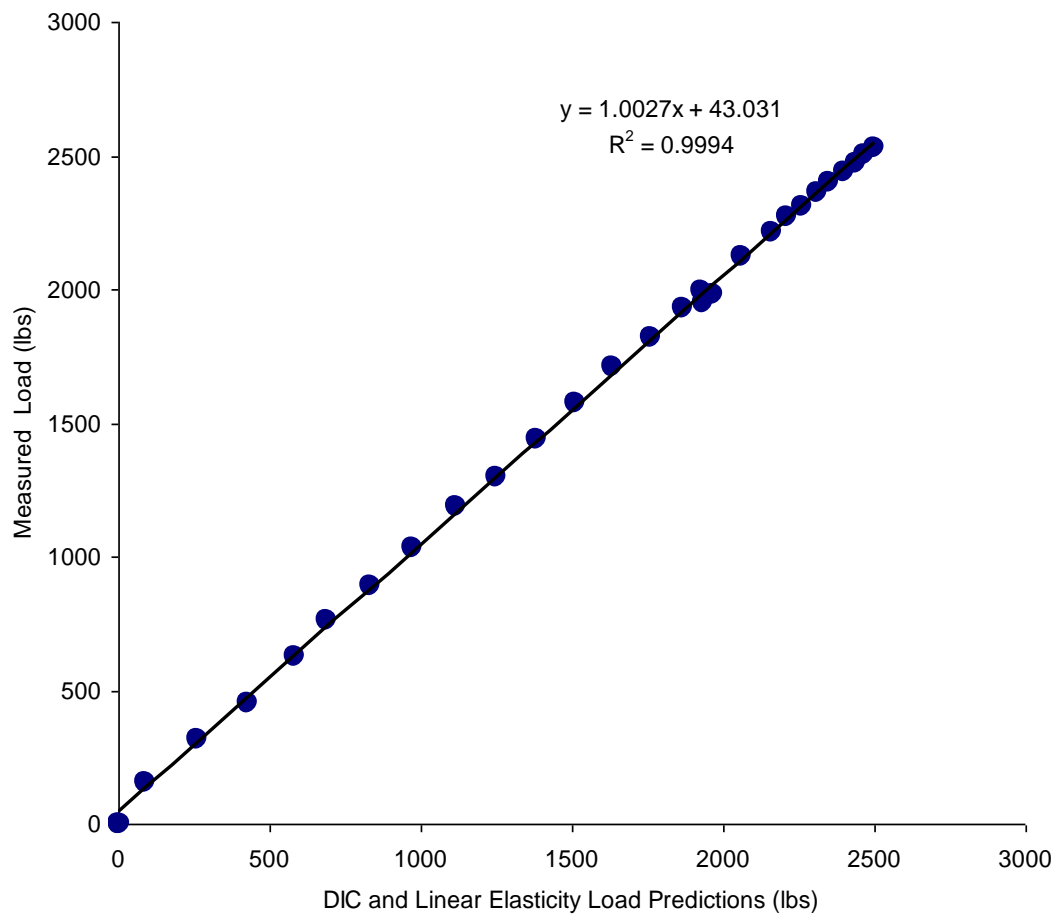


Figure 7. Measured and Calculated Loads for Coupon A2

Table 4 lists the linear material stiffness and interlaminar strength data for the finite element-based failure models of the wrinkle coupons.

Table 4. IM7/8552 Tape Stiffness and Strength Properties

Tensile Moduli (msi)	
$E_{11}$	22.3
$E_{22} = E_{33}$	1.3
Shear Moduli (msi)	
$G_{12} = G_{13}$	0.77
$G_{23}$	0.43
Poisson's Ratio	
$\nu_{12} = \nu_{13}$	0.32
$\nu_{23}$	0.5
Adhesive Ultimate Tensile Strain ( $\mu\epsilon$ )	8544
Interlaminar Tensile Strength $S_{33}$ (ksi)	14.3
Interlaminar Shear Strength $S_{13}$ (ksi)	16.4

Fracture toughness-corrected stress-based interlaminar strength data available in open literature [10] are used.

### 2.2.2 Nonlinear Interlaminar Shear Stress-Strain Relations

Test data for nonlinear interlaminar shear stress-strain response of IM7/8552 tape are presented in this section. Eight 36-ply unidirectional tape short-beam shear (SBS) coupons, manufactured to ASTM Standard specifications [15], were statically loaded (0.05 inches/minute head displacement rate) to failure. The SBS coupons are 1.5-inches-long, 0.26-inches-thick, and 0.2-inches-wide. Support length is 1 inch.

The DIC technique was used for assessment of stress-strain behavior. Figure 8 shows a SBS test coupon.

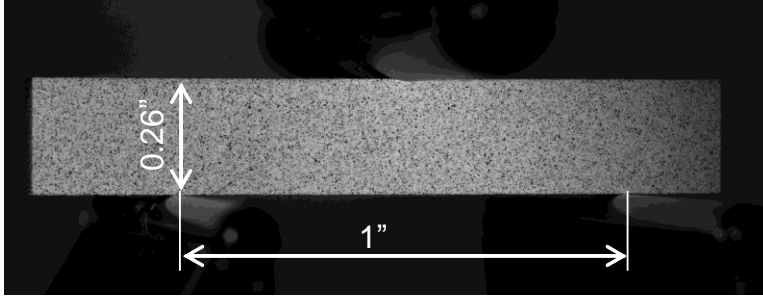


Figure 8. IM7/8552 Carbon/Epoxy Tape SBS Test Coupon

A random texture for DIC strain assessment was created using black and white spray paints. Figure 9 shows delamination failure.

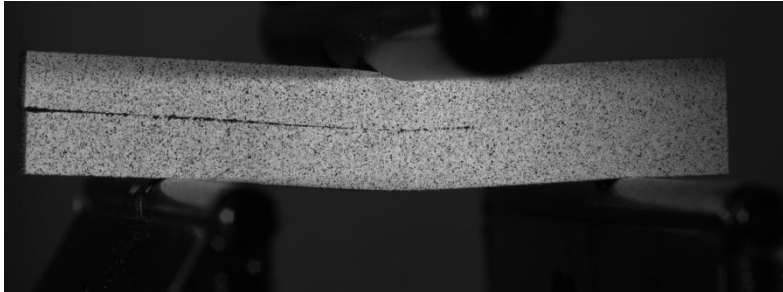


Figure 9. IM7/8552 Carbon/Epoxy SBS Coupon Failure

Figure 9 shows the interlaminar shear stress-strain response for the eight SBS coupons tested.



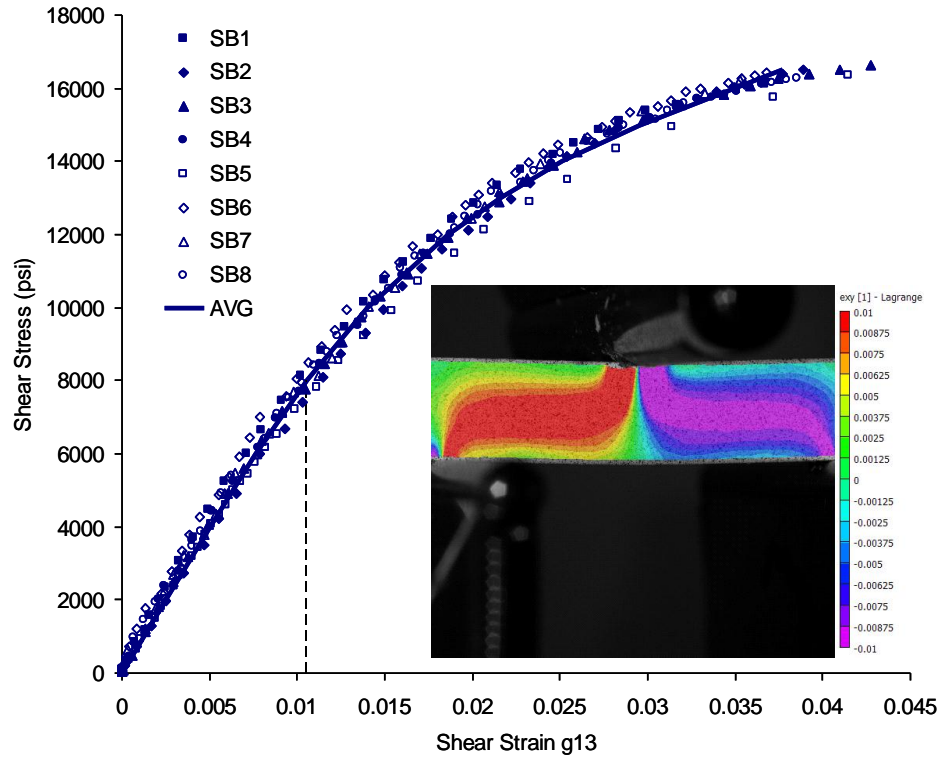


Figure 10. Shear Stress-Strain Response for Unidirectional IM7/8552 Tape Specimens

Ramberg-Osgood equations [4] fits the test data using a least squares approximation.

Equation 1 gives the expression for the strain-stress shear relation:

$$\gamma_{13} = \frac{\tau_{13}}{G_{13}} + \left( \frac{\tau_{13}}{K} \right)^{\frac{1}{n}} \quad (1)$$

Table 5 lists the values for the interlaminar shear strength  $S_{13}$  corresponding to the ultimate failure load, and linear shear modulus  $G_{13}$ , nonlinear modulus  $K$ , and exponent  $n$ . Average (AVG) values and coefficients of variation (COV) are also listed.

Table 5. Interlaminar Shear Strength and Stiffness Values

<b>Specimen</b>	<b>S<sub>13</sub> (psi)</b>	<b>G<sub>13</sub> (psi)</b>	<b>K (psi)</b>	<b>n</b>
<b>1</b>	16136	864172	39771	0.217628
<b>2</b>	16531	733521	37743	0.196601
<b>3</b>	16753	796205	37052	0.201165
<b>4</b>	16211	767530	35817	0.188536
<b>5</b>	16890	766088	38066	0.216761
<b>6</b>	16561	853828	35704	0.191663
<b>7</b>	16598	792083	41576	0.219112
<b>8</b>	16303	784294	36441	0.193697
<b>AVG</b>	<b>16498</b>	<b>794715</b>	<b>37771</b>	<b>0.203145</b>
<b>COV</b>	<b>1.59%</b>	<b>5.57%</b>	<b>5.38%</b>	<b>6.26%</b>

The trend line shown in Figure 10 is based on Table 3 AVG constants. For shear strain exceeding 1%, the IM7/8552 carbon/epoxy tape SBS specimens exhibit highly nonlinear interlaminar shear stress-strain behavior.

## 2.3 Finite Element Analysis for Large Wrinkle Coupons

### 2.3.1 ABAQUS Finite Element Model

#### 2.3.1.1 Plane Stress Mesh

Plane stress finite element-based failure models were built for B1, B2, and B3 wrinkle coupons in ABAQUS software. The models' geometry is created from digital pictures of the coupons presented on Figure 1. Series of points are picked up along the layers'

interfaces and a sketch is generated in ABAQUS with spline-lines passing through the points as illustrated on Figure 11.

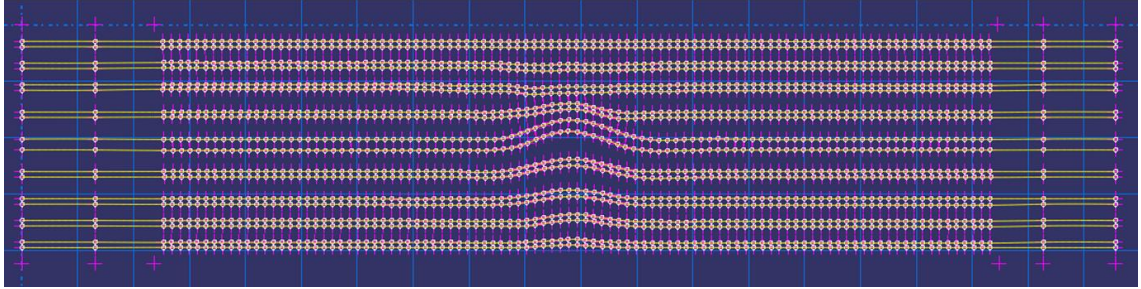


Figure 11. ABAQUS Sketch for Coupon B2 Geometry

A 2D plane stress structured finite element mesh is generated on the geometry. Figure 12 shows the finite element mesh for B2 wrinkle coupon with 100,000 4 nodes plane stress elements CPS4R with about 200,000 DOF.  $\pm 45$  deg. Plies have been colored in red and 0 deg. Plies in green.

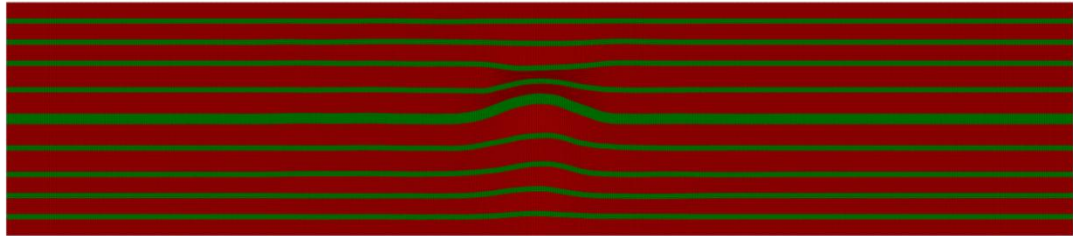


Figure 12. Plane Stress Finite Element Mesh for B2 Wrinkle Coupon

Table 4 lists the linear stiffness and interlaminar strength data, and Table 5 lists the parameters for the nonlinear interlaminar shear stress-strain response of IM7/8552 unidirectional tape. The  $\pm 45$ -degree plies are represented in the plane stress finite element model through effective stiffness properties. Coordinate transformation for stiffness tensor components [11] is used to obtain the linear stiffness constants. A ratio of the effective transverse shear modulus for  $\pm 45$ -degree plies and  $G_{13}$  shear modulus

for unidirectional tape scales the nonlinear shear stress-strain response for the  $\pm 45$ -degree ply-groups.

The boundary conditions include fixed displacements at the left end, and fixed transverse displacements and uniform axial displacements with applied tensile force at the right end.

### **2.3.1.2 Non-linear Interlaminar Shear Properties**

Non-linear interlaminar shear stress-strain relations are implemented using ABAQUS user subroutine USDFLD [16]. Material non-linearity response is modeled through a damage approach where the stiffness is gradually degraded by a damage variable  $d$ .

The expression for the shear stress-strain relation is given by Equation 3:

$$\sigma_{xy} = G_{xy} (1 - d) \gamma_{xy} \quad (2)$$

The damage variable  $d$  is a function of the shear strain and is calculated by the subroutine at each analysis time increment by using the strain state of the previous increment.

The simplest way to express the damage variable is to use the average strain-stress relation given by Equation 1 and extrapolate it by using a polynomial function in order to obtain the non-linear stress-strain relation. A 5-degree polynomial relation ensures an accurate representation. The stress-strain relation is expressed by Equation 4:

$$\sigma_{xy} = G_{xy} \gamma_{xy} + a \gamma_{xy}^2 + b \gamma_{xy}^3 + c \gamma_{xy}^4 + d \gamma_{xy}^5 \quad (3)$$

Numerical coefficients  $a, b, c$  and  $d$  for non-linear terms are determined using an interpolation software and are listed below:

$$\begin{aligned} a &= 5.11 \times 10^6 \text{ Psi} \\ b &= -1.15 \times 10^9 \text{ Psi} \\ c &= 2.85 \times 10^{10} \text{ Psi} \\ d &= -2.19 \times 10^{11} \text{ Psi} \end{aligned}$$

Equation 4 can be linearized to obtain the stress-strain relation at time increment  $i$ :

$$\sigma_{xy}[i] = G_{xy} \gamma[i] - a \gamma_{xy}[i-1] - b \gamma_{xy}[i-1]^2 - c \gamma_{xy}[i-1]^3 - d \gamma_{xy}[i-1]^4 \quad (4)$$

leading to the expression of damage variable:

$$d = \frac{-a \gamma_{xy}[i-1] - b \gamma_{xy}[i-1]^2 - c \gamma_{xy}[i-1]^3 - d \gamma_{xy}[i-1]^4}{G_{xy}} \quad (5)$$

This algorithm requires a time increment small enough to reach convergence. Figure 13 illustrates the convergence of the shear stress-strain relation for different time increment (time step = 1).

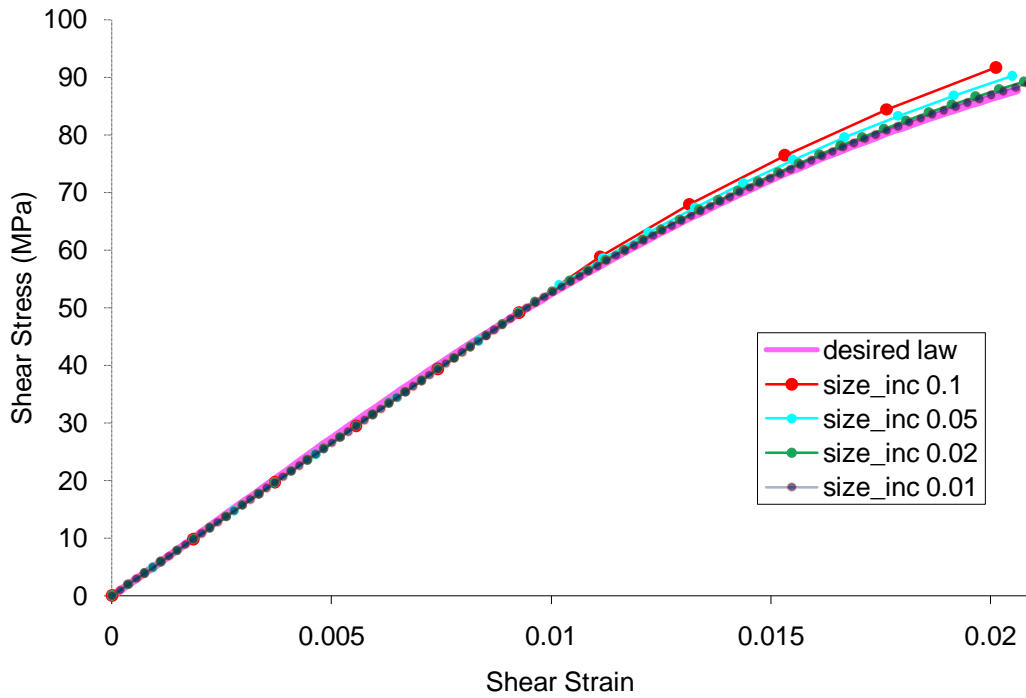


Figure 13. Convergence of USDFLD non-linear shear stress-strain algorithm

Convergence is reached for a time increment of 0.02 period time for the analysis (50 increments for a time period of 1).

### 2.3.1.3 Local Material Orientation

ABAQUS Fortran user-subroutine ORIENT [16] was used to assign local material orientation properties along the wrinkle directions. The subroutine uses the element nodes' coordinates to define a local coordinate system (X',Y') by rotating the global coordinate system (X,Y) of angle alpha as illustrated in Figure 14. A structured mesh with proper aspect ratio elements is necessary.

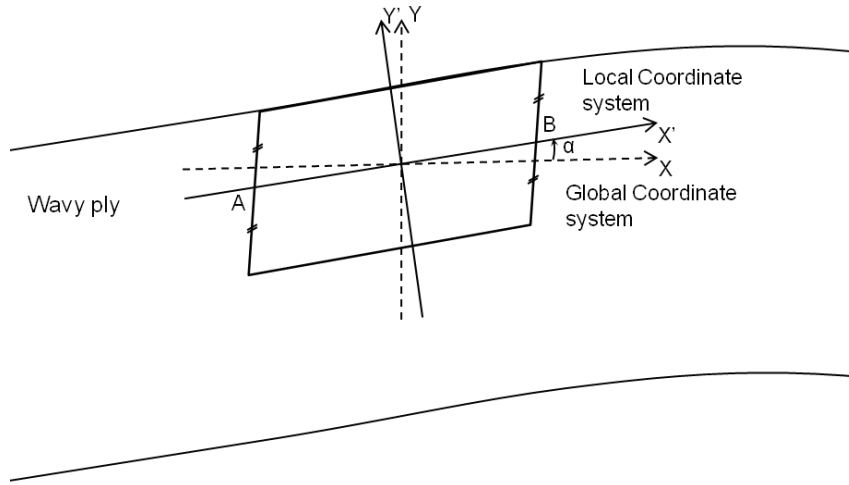


Figure 14. Element Based local Coordinate System

Angle alpha is calculated in the subroutine for each element by using the approximation:

$$\alpha = \text{atan} \left( \frac{Y_B - Y_A}{X_B - X_A} \right) \quad (6)$$

With A and B the respective mid-points of the 2 small sides of hexagonal plane stress elements CPSR4R. Figure 15 shows element local orientation systems generated at the main 0 deg. Ply wrinkle for coupon B2 FEM.

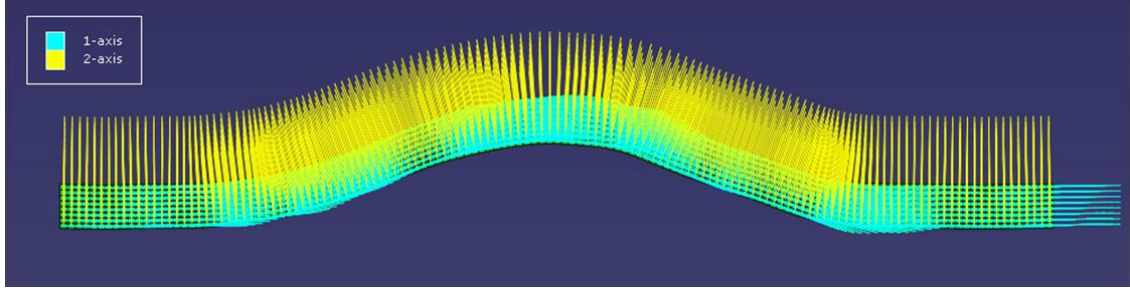


Figure 15. User Defined Orientation Systems at The Main Wrinkle for B2 FEM

### 2.3.2 Finite Element Predictions

Table 6 lists the failure load predictions for the wrinkle coupons based on the adhesive tensile strain, interlaminar tensile stress, and a mixed-mode stress (Hashin) failure criteria [17]. Criteria are defined as followed :

$$\text{Adhesive Tensile Strain : } \frac{\varepsilon_{33}}{e_{\max 33}} = 1 \quad \varepsilon_{33} > 0$$

$$\text{Interlaminar Tensile Stress : } \frac{\sigma_{33}}{S_{33}} = 1 \quad \sigma_{33} > 0$$

$$\text{Hashin : } \left( \frac{\sigma_{33}}{S_{33}} \right)^2 + \left( \frac{\sigma_{13}}{S_{13}} \right)^2 = 1 \quad \sigma_{33} > 0$$

where  $e_{\max 33}$  is the maximum admissible strain,  $S_{33}$  and  $S_{12}$  the interlaminar tensile and shear strengths. No matrix failure is supposed to occur for interlaminar compression.

FEM failure predictions are done for a linear model and a model where nonlinear interlaminar shear stress-strain responses are implemented.

Table 6. Failure Load Predictions for IM7/8552 Tape Wrinkle Coupons

Failure Criteria	Material Strength	Linear FEM	Nonlinear FEM
<b>B1</b>			
Interlaminar Tensile Strain	8,544 $\mu\epsilon$	4746 lbs	4252 lbs
Interlaminar Tensile Stress	$S_{33} = 14.3$ ksi	4631 lbs	4296 lbs
Mixed-Mode Stress $(\sigma_{33} / S_{33})^2 + (\tau_{13} / S_{13})^2 = 1$	$S_{33} = 14.3$ ksi	3061 lbs	3682 lbs
	$S_{13} = 16.4$ ksi		
<b>B2</b>			
Interlaminar Tensile Strain	8,544 $\mu\epsilon$	3872 lbs	3723 lbs
Interlaminar Tensile Stress	$S_{33} = 14.3$ ksi	4029 lbs	3763 lbs
Mixed-Mode Stress $(\sigma_{33} / S_{33})^2 + (\tau_{13} / S_{13})^2 = 1$	$S_{33} = 14.3$ ksi	2709 lbs	3359 lbs
	$S_{13} = 16.4$ ksi		
<b>B3</b>			
Interlaminar Tensile Strain	8,544 $\mu\epsilon$	4939 lbs	4541 lbs
Interlaminar Tensile Stress	$S_{33} = 14.3$ ksi	4499 lbs	4223 lbs
Mixed-Mode Stress $(\sigma_{33} / S_{33})^2 + (\tau_{13} / S_{13})^2 = 1$	$S_{33} = 14.3$ ksi	3026 lbs	3905 lbs
	$S_{13} = 16.4$ ksi		

The different failure criteria are evaluated and plotted using ABAQUS user subroutine UVARM. Figure 16 – Figure 18 and Figure 19 – Figure 21 present contours plots for Hashin and Interlaminar Tensile Stress (ITS) failure criteria when delamination onset is detected (failure criterion reaches one).



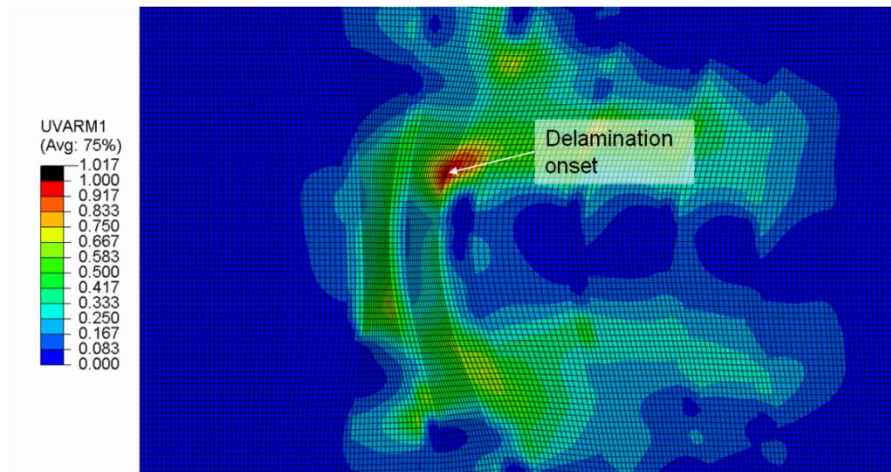


Figure 16. Hashin Criterion Contour Plot for Coupon B1 at 3682lbs Tension

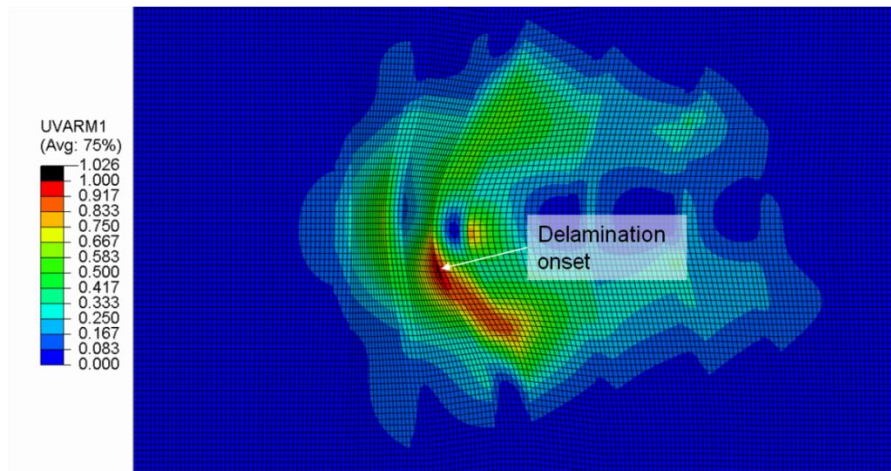


Figure 17. Hashin Criterion Contour Plot for Coupon B2 at 3360lbs Tension

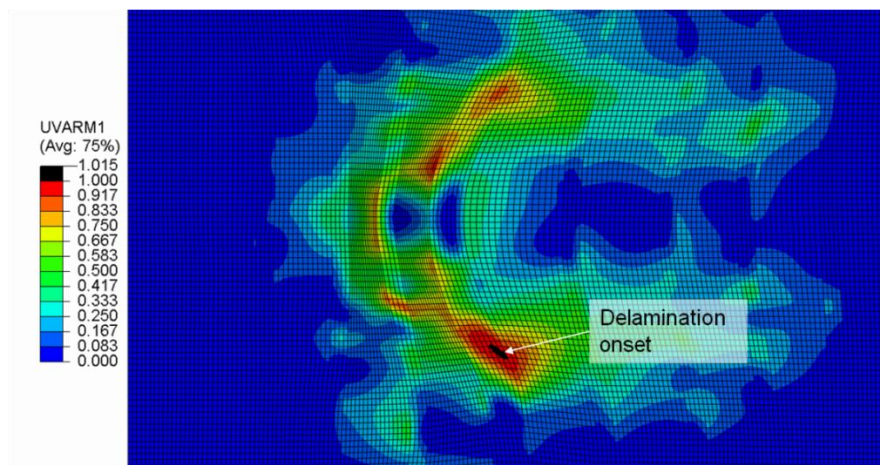


Figure 18. Hashin Criterion Contour Plot for Coupon B3 at 3905lbs Tension



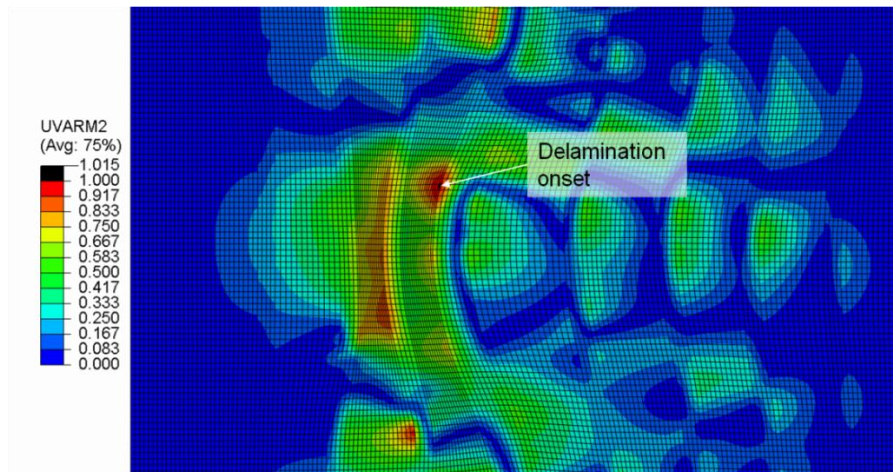


Figure 19. ITS Criterion Contour Plot for Coupon B1 at 4296lbs Tension

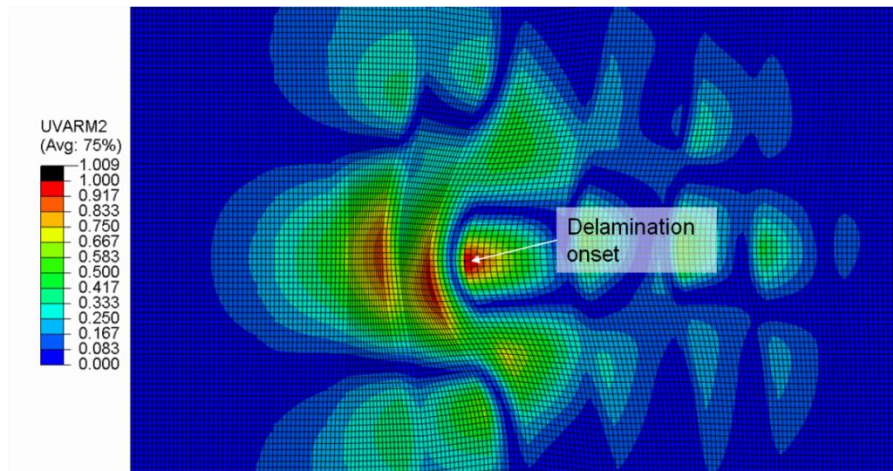


Figure 20. ITS Criterion Contour Plot for Coupon B2 at 3763lbs Tension

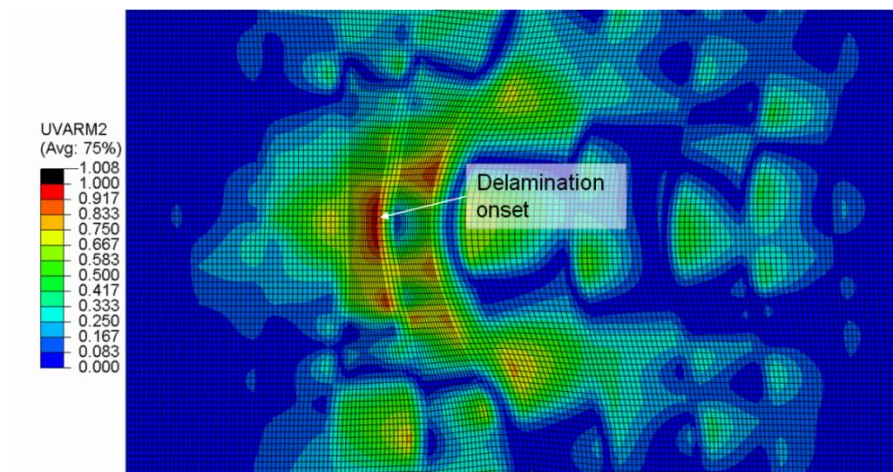


Figure 21. ITS Criterion Contour Plot for Coupon B3 at 4223lbs Tension

Predicted delamination sites are detected at different locations for the coupons and depend on which damage index is considered. However, delamination is predicted to occur mainly at the interface between  $[\pm 45]_4$  and  $[0]_4$  ply-groups along the largest (main) wrinkle. For coupon B1 delamination initiation due to combined effects of shear and tensile stresses (Hashin) is expected to occur first and on the right side of the main  $[\pm 45]_4$  wrinkle as shown on Figure 16. The same location is predicted if only Interlaminar Tensile Stress (ITS) is considered, but predicted failure load is higher (Figure 19). For coupon B2, location of the initial crack is predicted using the Hashin criterion on the right side of the main wrinkle and on the left side if ITS is considered. For coupon B3 the first crack is expected to occur at the left side of the main wrinkle based on the Hashin mixed-mode failure criterion. If only Mode I delamination (ITS) is considered, it is supposed to occur for coupon B3 at the left  $[\pm 45]_4$  interface of the  $[0]_4$  ply-group next to the main wrinkle.

### 2.3.3 Test Data Comparison

The large-wrinkle coupons B1, B2, and B3 were statically (0.05 inches/minute head displacement rate) loaded to failure. The DIC full-field measurement technique was used to monitor surface strains. Table 7 lists the cross-section dimensions and loads corresponding to the delamination failure.

Table 7. Cross-Section Dimensions and Failure Loads for Large-Wrinkle Coupons

Test Specimen	W (in)	T (in)	Failure Load (lbs)
B1	0.6413	0.1244	4227 to 4248
B2	0.64	0.1261	3544 to 3550
B3	0.6402	0.1263	4097 to 4101

Figure 22 – Figure 24 show the interlaminar strain contour plots for the three coupons B1,B2 and B3 just before delamination onset and compares test data to FEM results for nonlinear models. A good match between simulated strain contour plot DIC test results is important to validate the accuracy of nonlinear FEM models using the nonlinear interlaminar shear stress-strain relations.

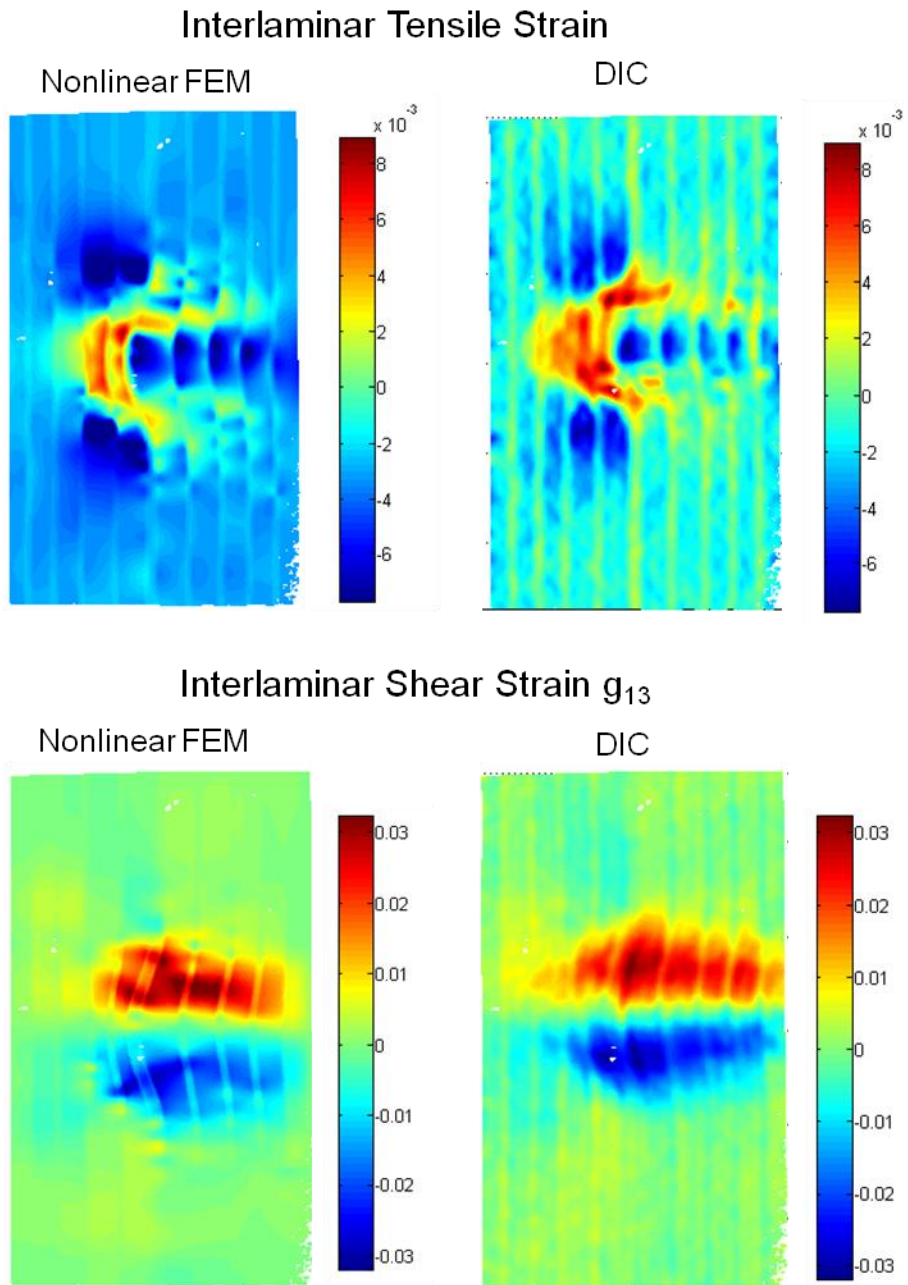


Figure 22. Interlaminar Strain Contour Plots for Coupon B1 at 4227 lbs Tension

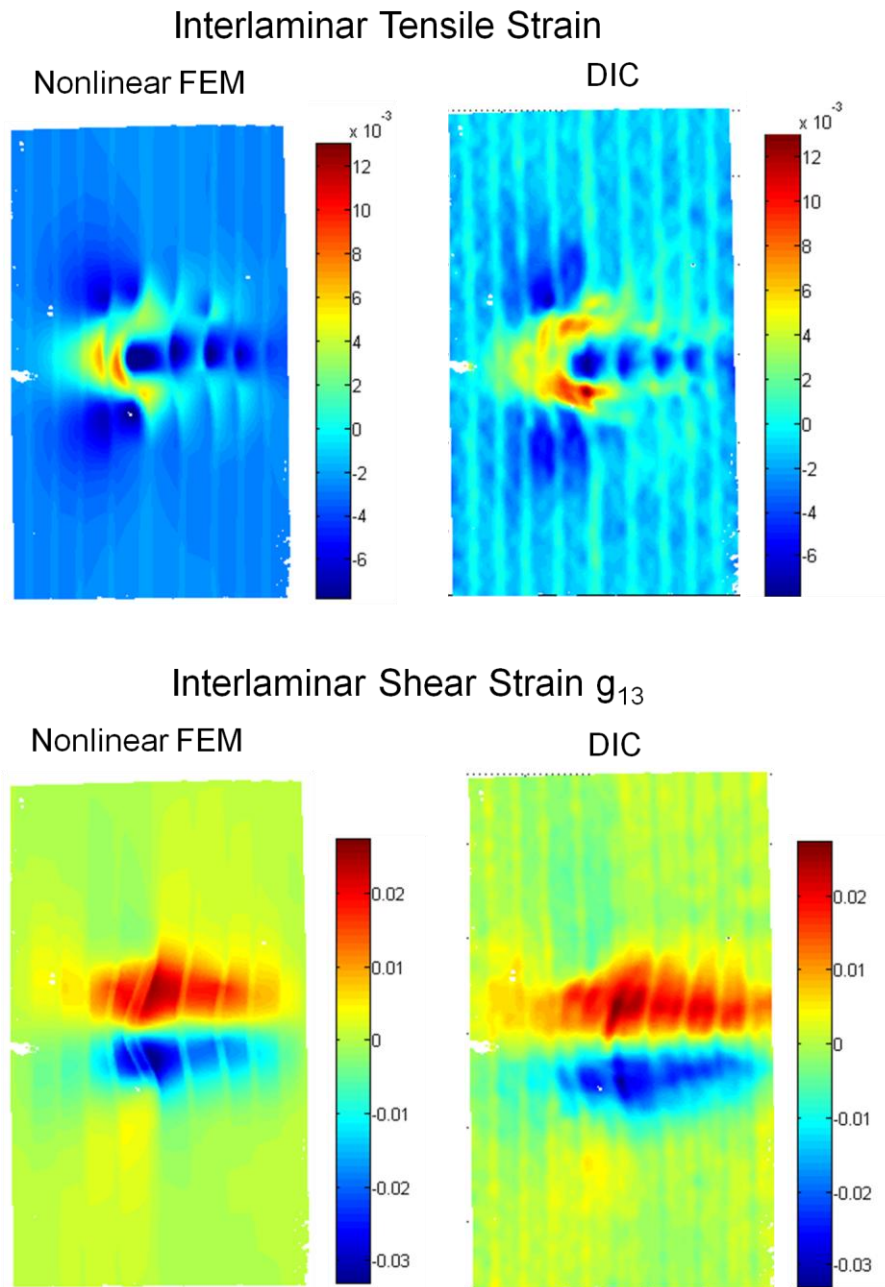


Figure 23. Interlaminar Strain Contour Plots for Coupon B2 at 3544 lbs Tension



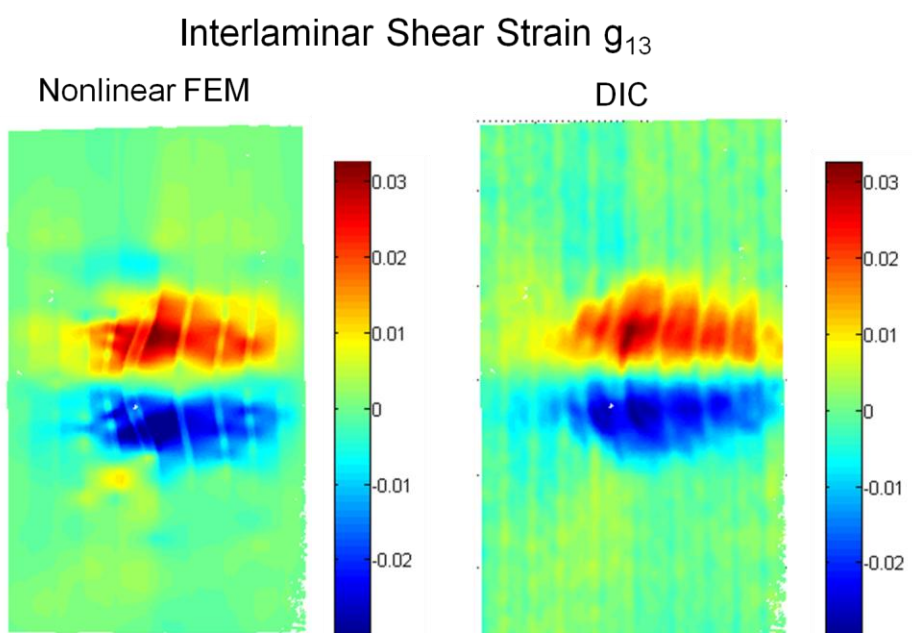
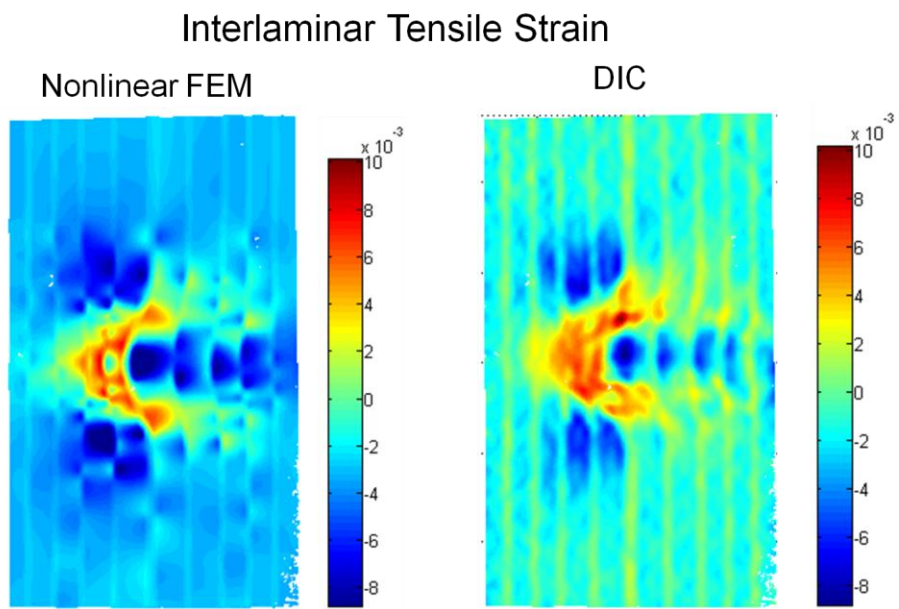


Figure 24. Interlaminar Strain Contour Plots for Coupon B3 at 4097lbs Tension

Interlaminar strain FEM predictions and measurements are in good agreement for the three coupons. This proves the capability of finite element models developed to be able to generate accurate failure previsions.

Figure 25-Figure 30 show test data (DIC) for Lagrange strain tensor components for the three coupons B1, B2 and B3 just before delamination and after delamination was detected. Delaminations for all coupons occur at the largest wrinkle between  $[\pm 45]_4$  and  $[0]_4$  ply-groups as expected.

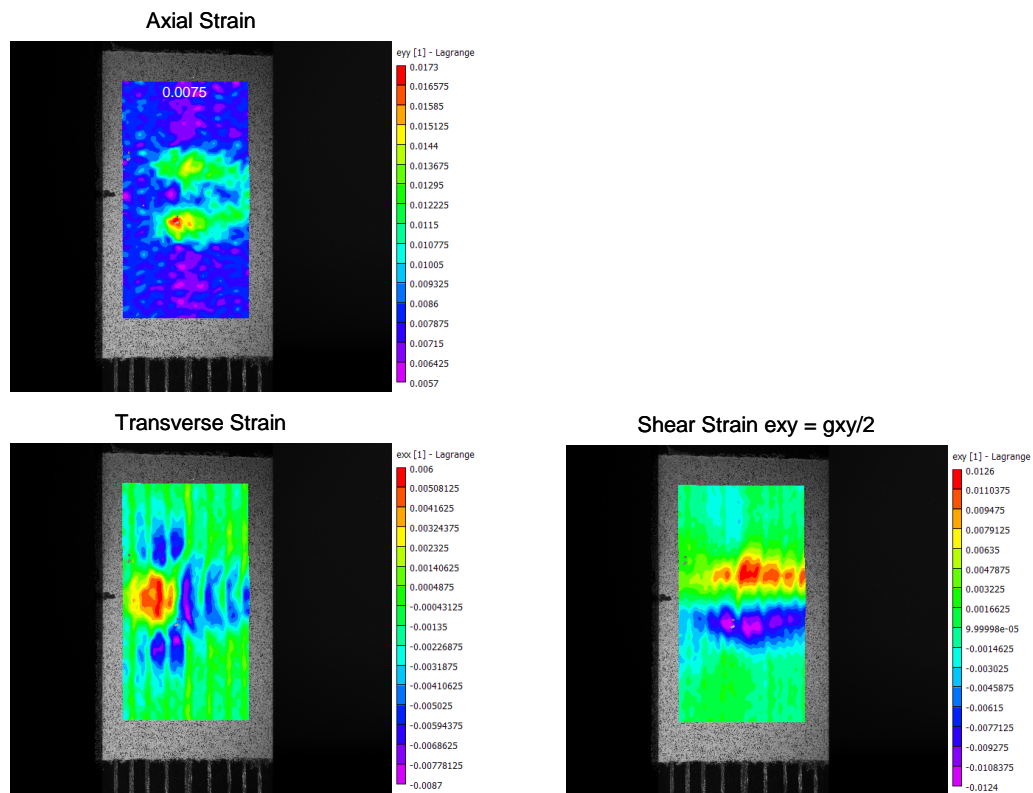


Figure 25. Lagrange Strain Contour Plots for Coupon B1 at 4227 lbs Tension



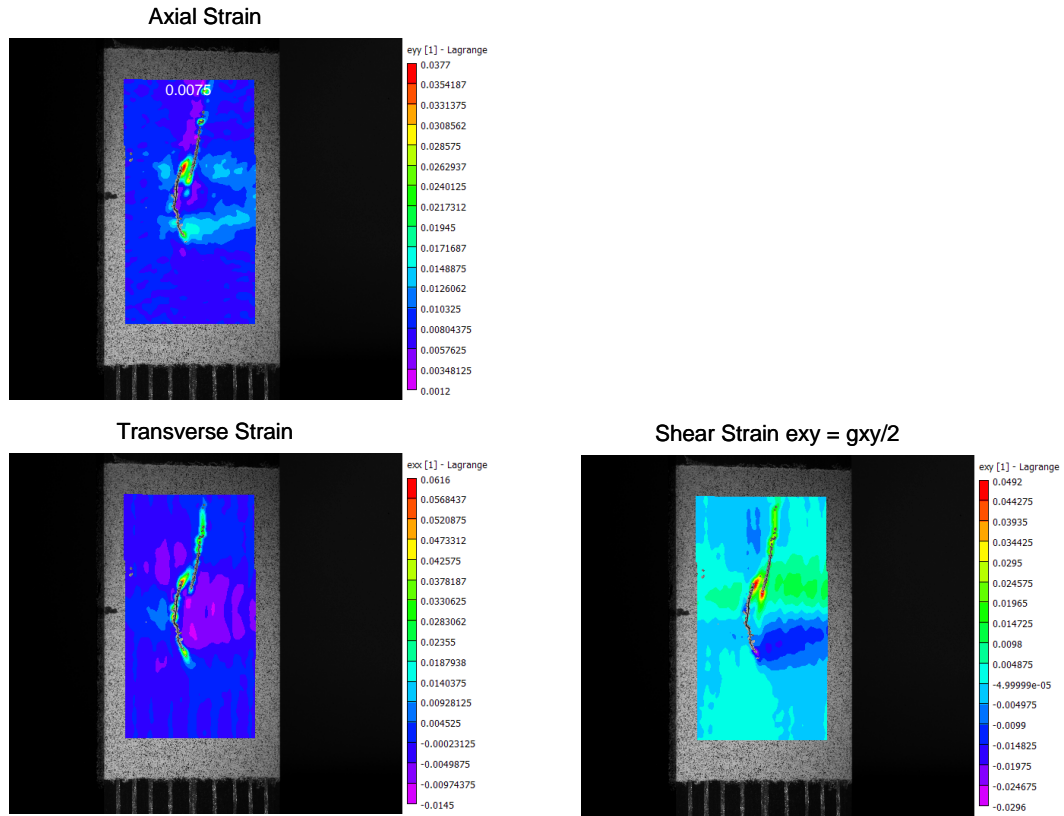


Figure 26. Lagrange Strain Contour Plots for Coupon B1 at 4248 lbs Tension

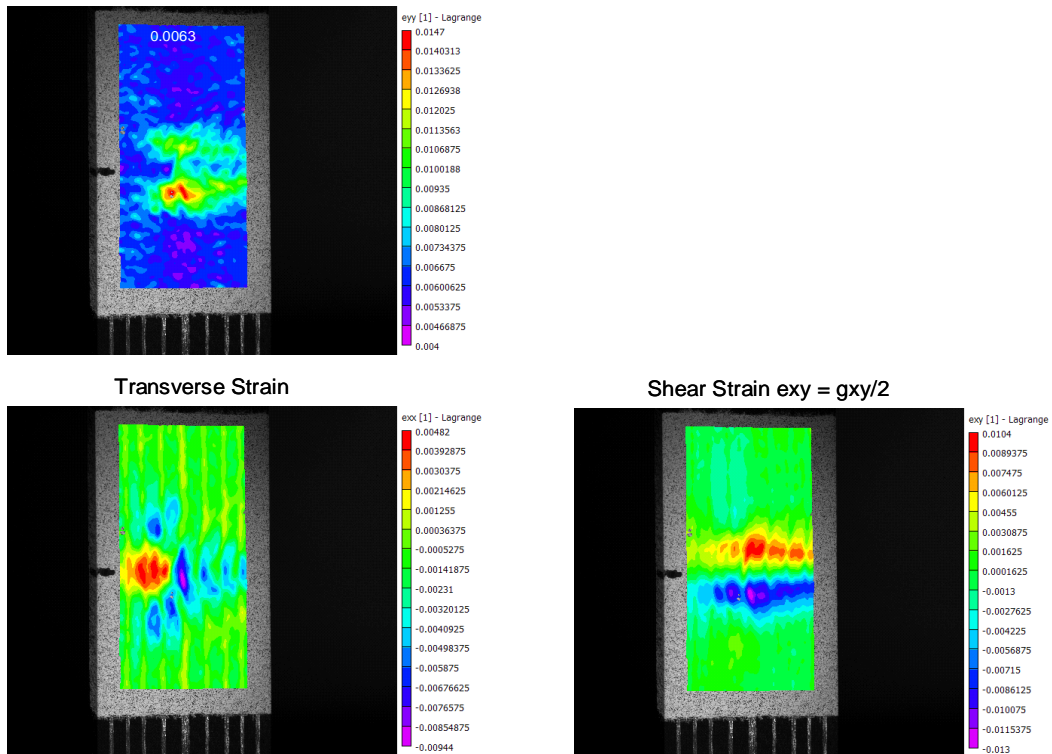


Figure 27. Lagrange Strain Contour Plots for Coupon B2 at 3544 lbs Tension

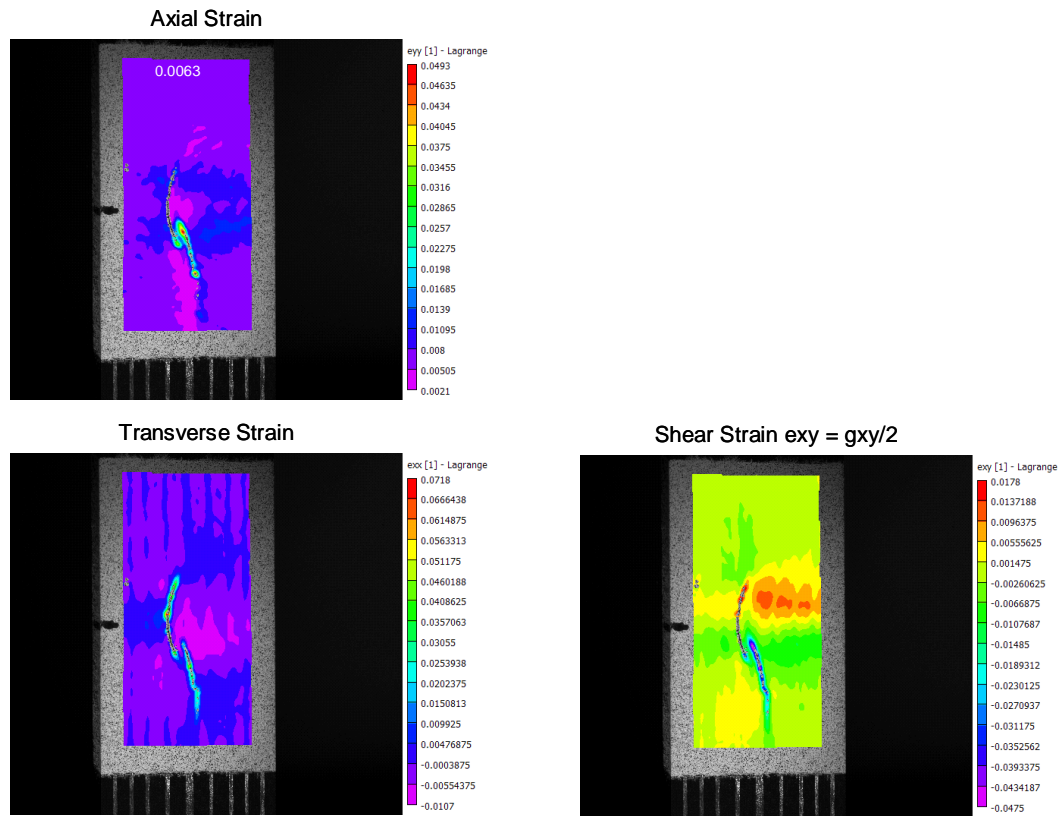


Figure 28. Lagrange Strain Contour Plots for Coupon B2 at 3550 lbs Tension

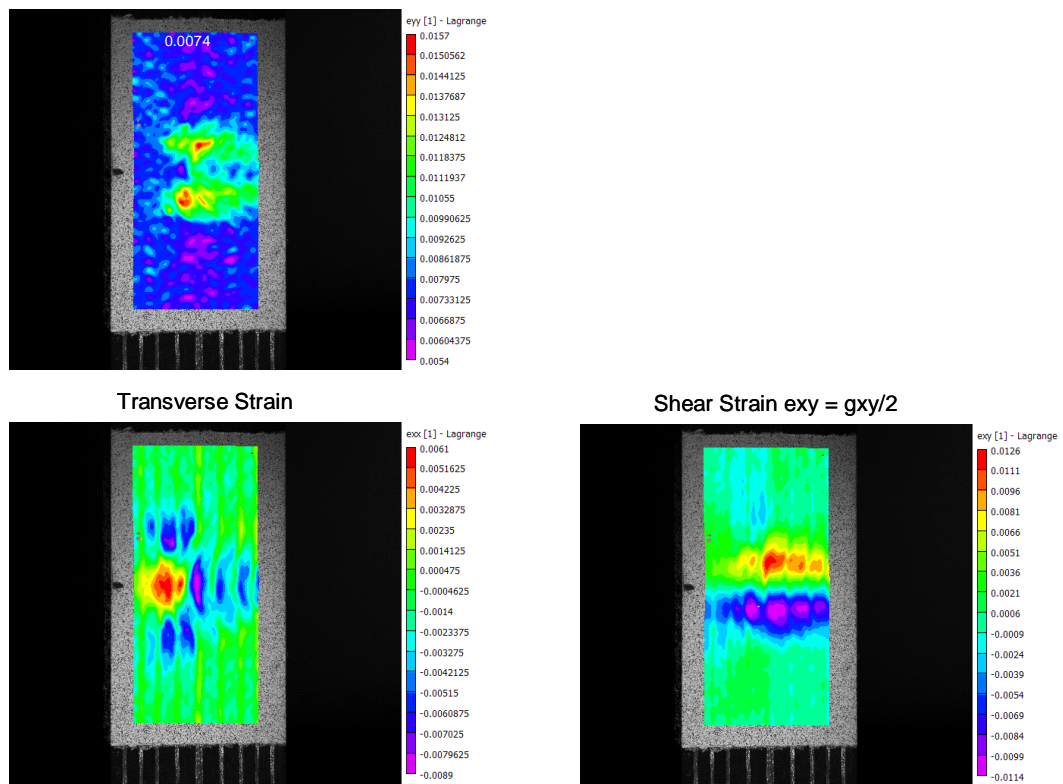


Figure 29. Lagrange Strain Contour Plots for Coupon B3 at 4097 lbs Tension

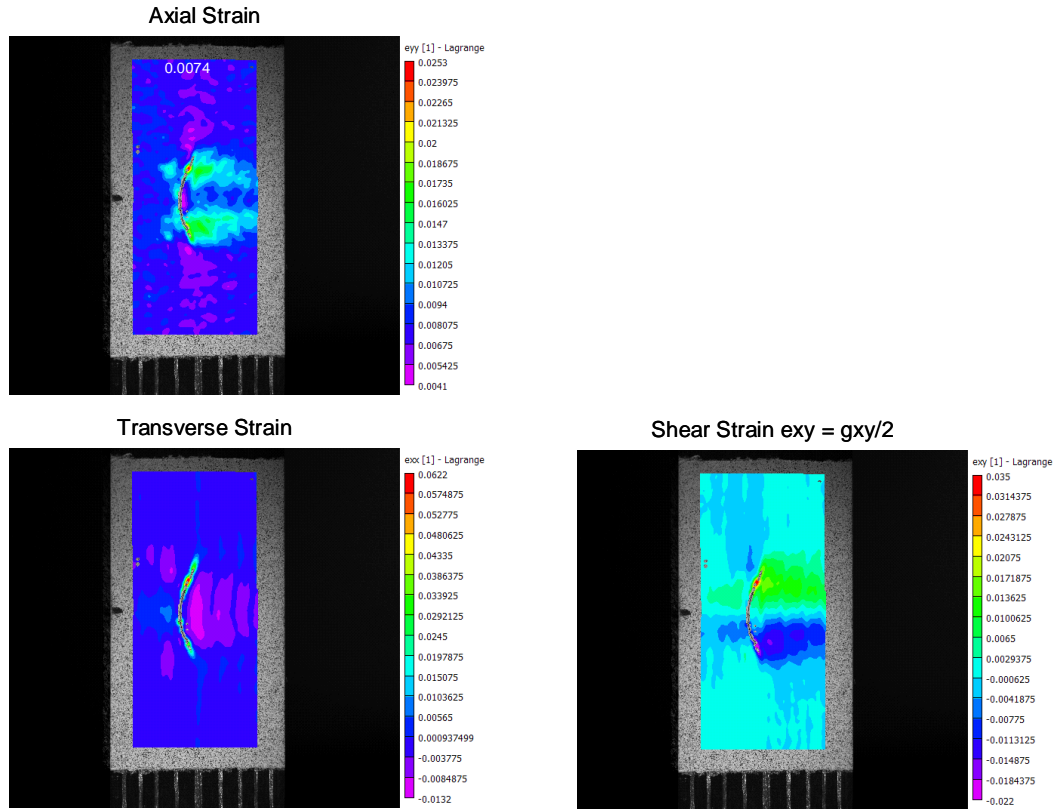


Figure 30. Lagrange Strain Contour Plots for Coupon B3 at 4101 lbs Tension

Figure 26 and Figure 28 show that two delamination cracks occur on different sides of the main wrinkle for B1 and B2 test specimens. This is consistent with the FEM predictions. Predictions for coupon B3 seem to be less accurate in term of the capacity to pick up the delamination onset location since failure was supposed to occur at the right side of the main wrinkle and not the left side (according to the Hashin criterion).

Table 8 summarizes the finite element-based failure load predictions and test data for all wrinkle coupons. Results from linear models are also included for comparison.

Table 8. Summary of Predictions and Test Data for Wrinkle Coupons

Failure Criteria	Material Strength	Linear FEM Failure Load Predictions (Error)	Nonlinear FEM Failure Load Predictions (Error)	Failure Load
<b>B1</b>				
Adhesive Tensile Strain	8,544 $\mu\epsilon$	4746 lbs (12%)	4252 lbs (0.1%)	4248 lbs
Interlaminar Tensile Stress	$S_{33} = 14.3$ ksi	4631 lbs (9%)	4296 lbs (1%)	4248 lbs
Mixed-Mode Stress $(\sigma_{33} / S_{33})^2 + (\tau_{13} / S_{13})^2 = 1$	$S_{33} = 14.3$ ksi $S_{13} = 16.6$ ksi	3061 lbs (-28%)	3682 lbs (-13%)	4248 lbs
<b>B2</b>				
Adhesive Tensile Strain	8,544 $\mu\epsilon$	3872 lbs (9%)	3723 lbs (5%)	3550 lbs
Interlaminar Tensile Stress	$S_{33} = 14.3$ ksi	4029 lbs (14%)	3763 lbs (6%)	3550 lbs
Mixed-Mode Stress $(\sigma_{33} / S_{33})^2 + (\tau_{13} / S_{13})^2 = 1$	$S_{33} = 14.3$ ksi $S_{13} = 16.6$ ksi	2709 lbs (-24%)	3359 lbs (-5%)	3550 lbs
<b>B3</b>				
Adhesive Tensile Strain	8,544 $\mu\epsilon$	4939 lbs (20%)	4541 lbs (11%)	4101 lbs
Interlaminar Tensile Stress	$S_{33} = 14.3$ ksi	4499 lbs (10%)	4223 lbs (3%)	4101 lbs
Mixed-Mode Stress $(\sigma_{33} / S_{33})^2 + (\tau_{13} / S_{13})^2 = 1$	$S_{33} = 14.3$ ksi $S_{13} = 16.6$ ksi	3026 lbs (-26%)	3905 lbs (-5%)	4101 lbs

The nonlinear interlaminar stress-strain relations enable significant improvement of the delamination onset prediction. Hashin criterion predicts the lowest (most conservative) failure load as expected, since combined effects of Tensile (mode I) and Shear (mode II) are taken into account. Predictions based on the mixed-mode Hashin criterion lead to conservative failure loads with an average error of 7.8% for nonlinear models (26% for linear models). The ITS criterion provides failure loads prevision with an average 3.3% error to the tests results. However the loads are non-conservative and the criterion did not seem to be able to predict accurately the crack location for coupon B3. We conclude that Hashin criterion appears to be the most appropriate for design.

## 2.4 Finite Element Analysis for Small Wrinkle Coupons

### 2.4.1 ABAQUS Finite Element Model

Finite elements models for small wrinkle coupons are built in the same way than large wrinkle coupons. Four nodes plane stress elements CPS4R are used to generate structured finite element meshes of the coupons. Models include about 260,000 Degrees of Freedom. Figure 31 shows the finite element mesh generated for small-wrinkle coupon C1. Similar meshes were built for the 12 coupons. Elements for 90 deg. Plies are colored in green and  $\pm 45$  deg plies in red.

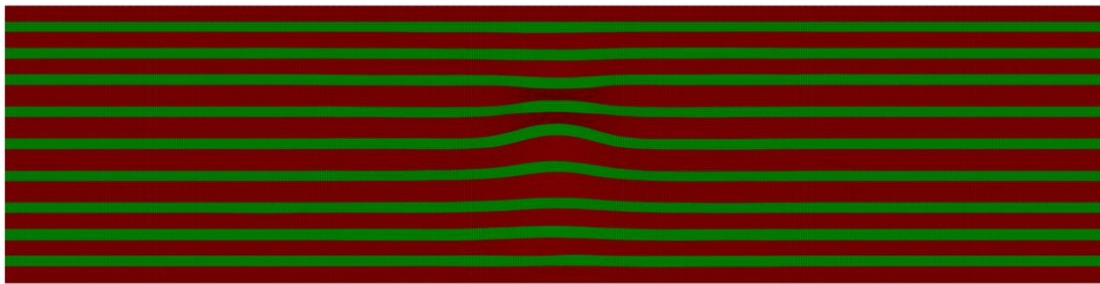


Figure 31. Plane Stress Finite Element Mesh for Coupon C1

ABAQUS user-defined subroutines are used to implement local material orientation systems along the wrinkles, to assign nonlinear interlaminar shear stress-strain relations for material IM7/8552 and to plot the different damage indexes. Porosity defects mentioned earlier and visible on Figure 3 are not taken into account in the models.

## 2.4.2 Finite Element Predictions

Failure loads were predicted for the 12 IM7/8552 tape small-wrinkle coupons using the Interlaminar Tensile Stress and Mixed-Modes Stress (Hashin) failure criteria. Table 9 lists failure loads using nonlinear FEM models for the specimens.

Table 9. Failure Load Predictions for IM7/8552 Tape Small Wrinkle Coupons

Specimens	Hashin Criterion Predicted Failure Load (lbs)	ITS Criterion Predicted Failure Load (lbs)
C1	9377	9570
C2	8061	9323
C3	8700	8990
C4	9199	9793
C5	8700	8990
C6	9280	9667
C7	9712	10015
C8	8546	9420
C9	9105	10116
C10	8158	9032
C11	9793	9793
C12	8838	8838

As expected predicted failure loads for delamination are higher than for the large wrinkle coupons (predicted loads from 3360 lbs to 4296 lbs) because of larger thickness and lower height-to-length aspect ratio for the wrinkles.

Contour plots of Hashin and Interlaminar Tensile Stress criteria provide expected locations of the delamination onsets around the main wrinkle. Figure 32 – Figure 34 Show contour plots for Hashin and ITS criteria at predicted failure loads.



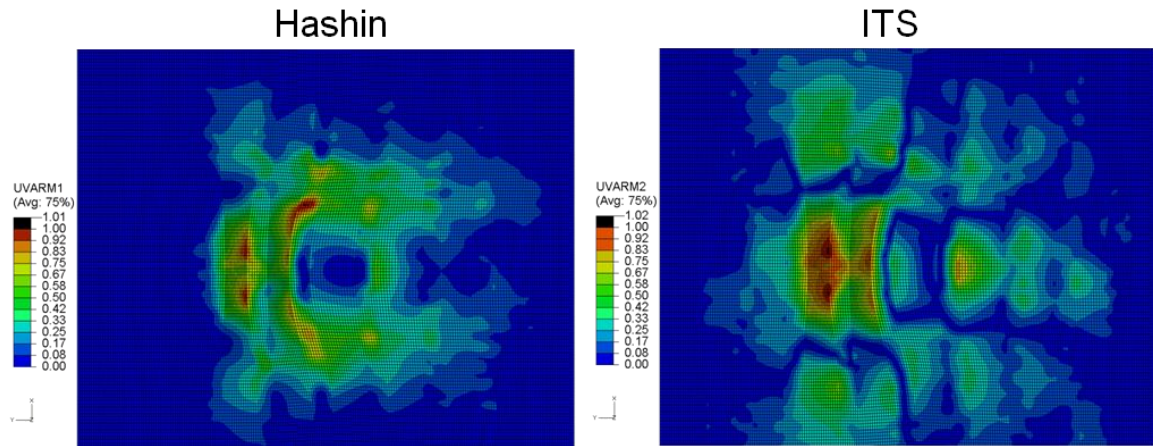


Figure 32. Hashin and ITS Contour Plots for Coupon C1 at Predicted Failure Loads

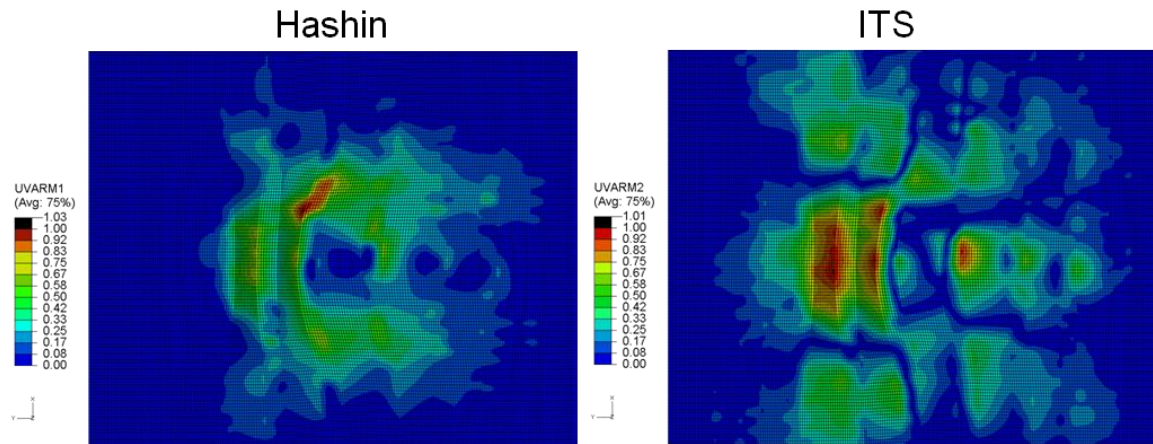


Figure 33. Hashin and ITS Contour Plots for Coupon C2 at Predicted Failure Loads

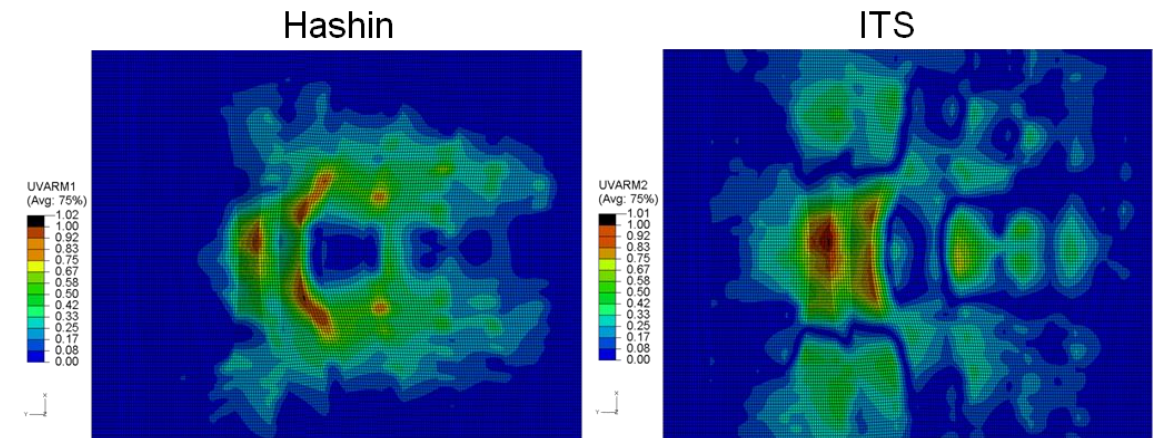


Figure 34. Hashin and ITS Contour Plots for Coupon C3 at Predicted Failure Loads

Similar to the large wrinkle coupons, delamination onsets is expected to occur at one of the interface of the main  $[\pm 45]_8$  wrinkle and the neighboring group of  $[0]_4$  ply.

### **2.4.3 Test Data Comparison**

Figure 35 – Figure 37 compares the FEM predictions and test data (DIC) for transverse and shear strains in the coupons C1, C2 and C3 at low tension loads before delamination.



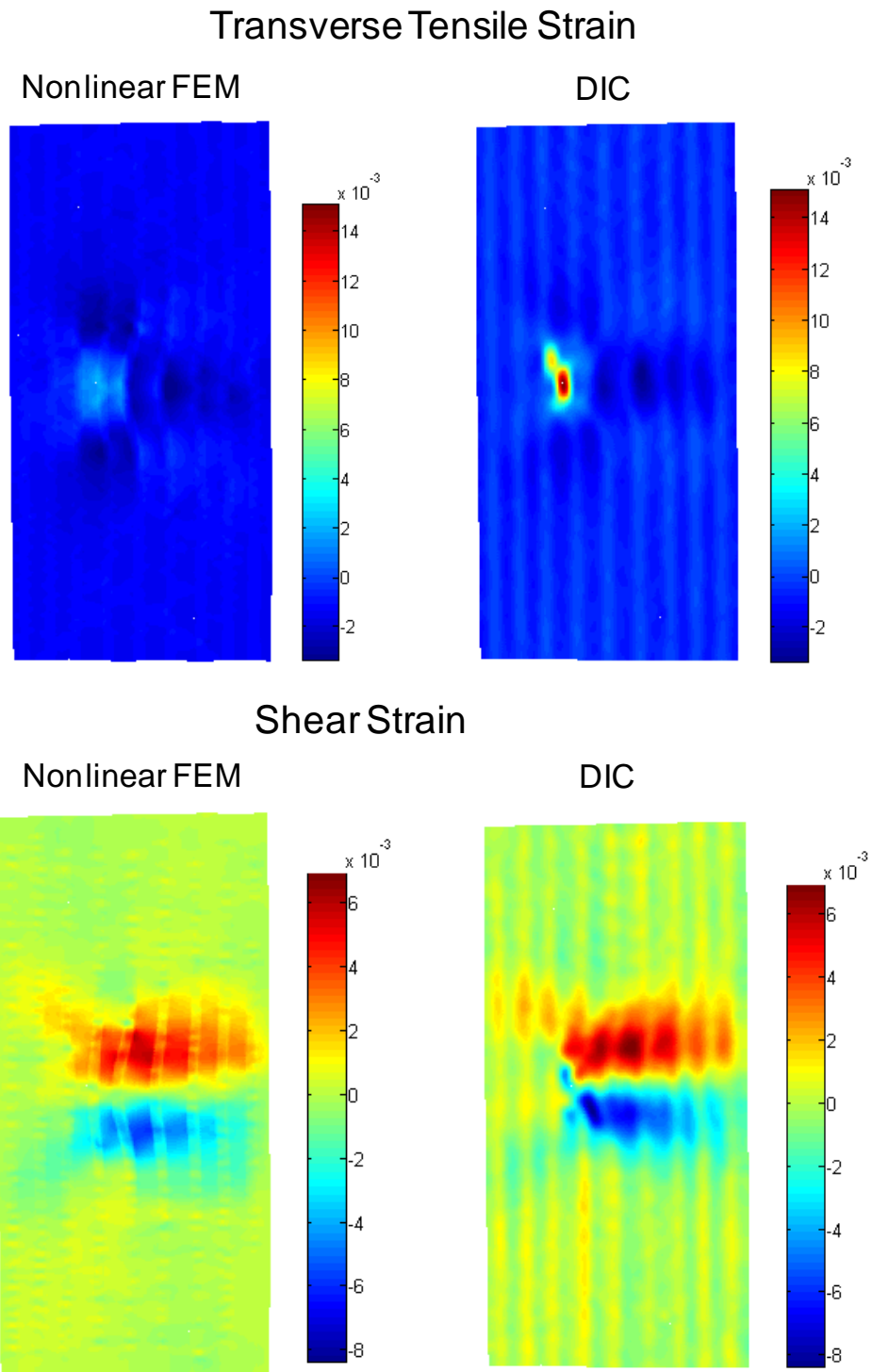


Figure 35. Strain Contour Plots for Coupon C1 at 3086lbs Tension

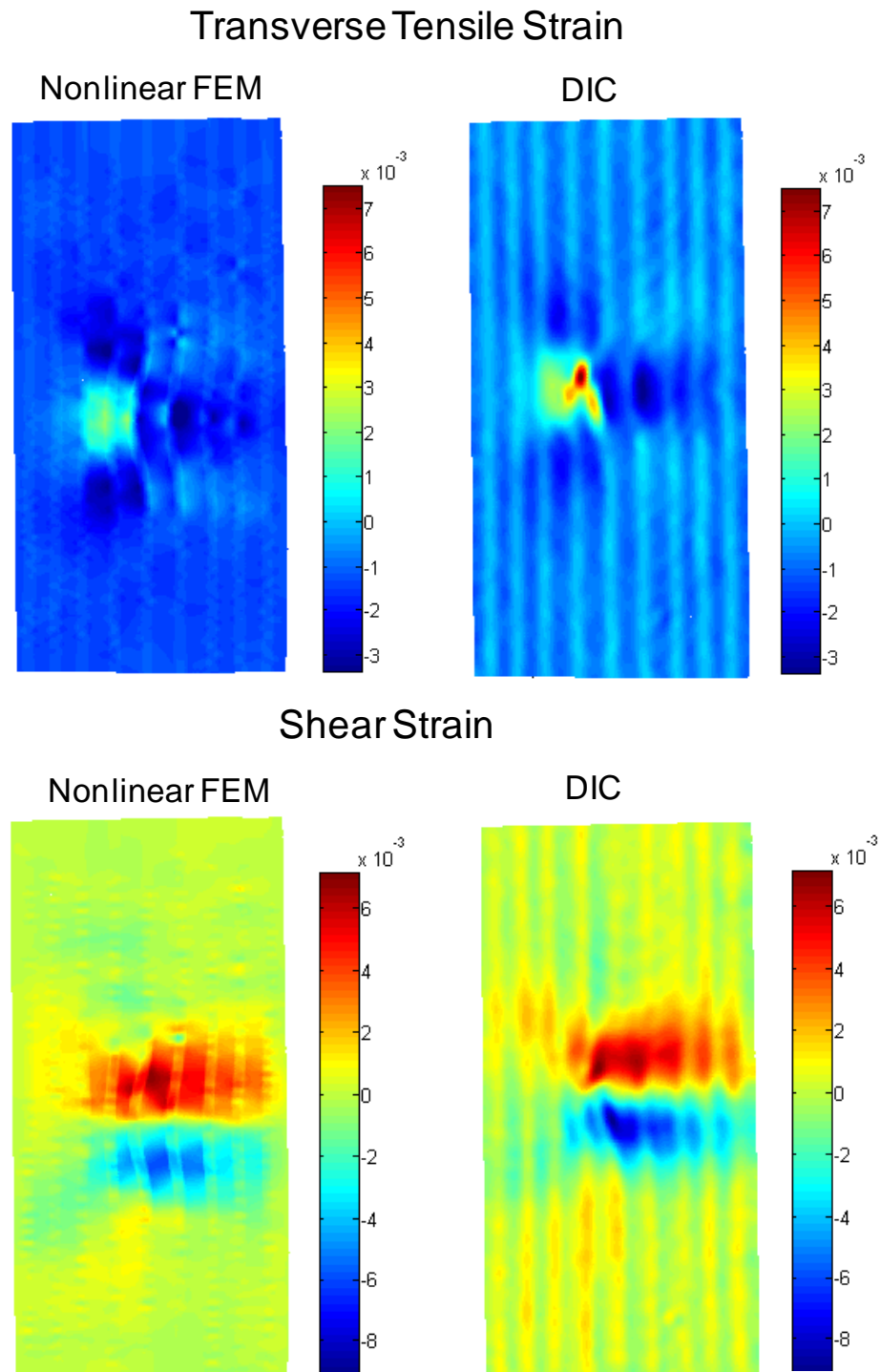


Figure 36. Strain Contour Plots for Coupon C2 at 3129lbs Tension

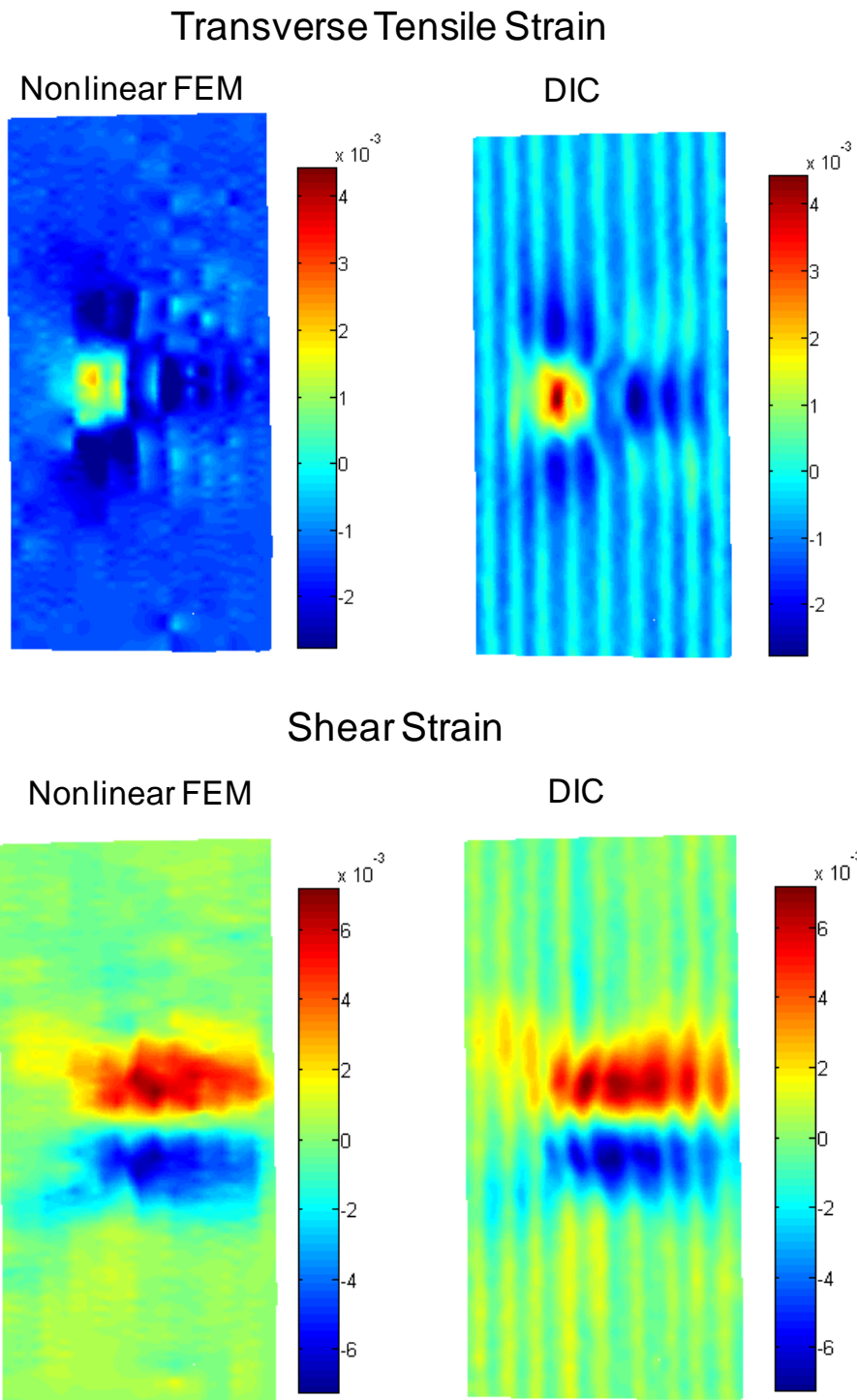


Figure 37. Strain Contour Plots for Coupon C3 at 3156lbs Tension

Table 10 compares maximum strains.

Table 10. Test Data and FEM Predictions for Maximum Strains

	<b>E11</b>	<b>E22</b>	<b>E12</b>
<b>C1 (at 3086 lbs)</b>			
Tests ( $\mu\epsilon$ )	5.42	15.01	6.88
FEM ( $\mu\epsilon$ )	4.86	2.24	6.12
Error (%)	-11.5	-570	-12.4
<b>C2 (at 3129 lbs)</b>			
Tests ( $\mu\epsilon$ )	5.63	7.48	7.13
FEM ( $\mu\epsilon$ )	5.28	2.35	6.88
Error (%)	-6.63	-68.6	-3.63
<b>C3 (at 3156 lbs)</b>			
Tests ( $\mu\epsilon$ )	5.51	4.41	7.13
FEM ( $\mu\epsilon$ )	5.19	2.55	6.97
Error(%)	-6.16	-72.9	-2.89

Although the interlaminar shear strains in Figure 35 – Figure 37 are in agreement, the difference in the transverse tensile strain E22 is significant. DIC contour plots for E22 show high strain concentration spots that are not predicted by the FEM. Table 10 shows that the maximum transverse tensile strain appeared to be up to 6.7 times higher in tests than in FEM predictions for coupon C1. Similar observations can be done for the other coupons.

A further examination of the DIC results shows that locations of high strain concentrations seem to correspond to locations of porosity voids mentioned earlier on the different coupons. Figure 38 illustrates that correspondence for coupon C1.

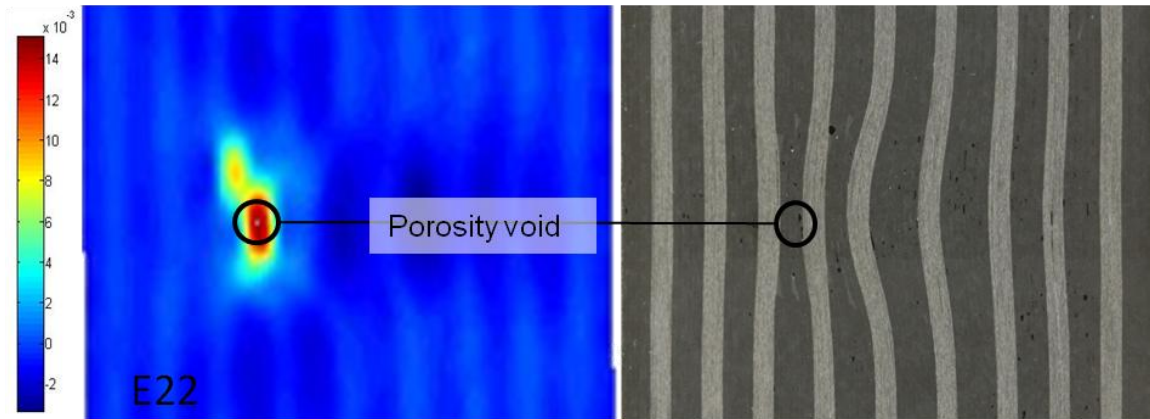


Figure 38. High Strain Concentration Due to Porosity Void for Coupon C1

Porosity consists in the accidental inclusion of interfacial voids in the matrix that will result into local stress and strain concentrations. Thus, the differences between FEM and tests results could be explained by the presence of this defect which was not included in the finite element models. As shown in Figure 38, porosity voids are present in the wrinkle area with high stress gradients. Delaminations will initiate at these designated locations and at much lower loads than expected because of stress concentrations.

Table 11 summarizes the results for predicted and tests data failure loads for the first three coupons.

Table 11. Predicted and Tested Failure Loads for Small Wrinkle Coupons

Specimens	Hashin Criterion Predicted Failure Load (lbs)	ITS Criterion Predicted Failure Load (lbs)	Tests Failure loads (lbs)
C1	9377	9570	3221
C2	8061	9323	3257
C3	8700	8990	3281

Failure occurs for the three coupons at loads between 3221 lbs and 3281 lbs, which is very far from what has been predicted (around 9000 lbs). We can also point out, that these failure loads are significantly lower than failure loads observed on large wrinkle coupons; contrary to what could be expected.

Inclusion of models for porosity appears to be crucial in order to obtain accurate failure predictions.

## **2.4.4 Suggestions to Assess the Porosity Problem**

### **2.4.4.1 *Modifying the Geometry***

Since porosity voids appear to be visible on the surface of the coupons, a possible solution could be the direct modification of the geometry in ABAQUS models to include the presence of voids. Including geometric voids will simulate stress and strain concentrations. Concentration factors are functions of the discontinuity's geometry. For a crack of length  $2a$  and width  $2b$ , the stress concentration factor under an applied external stress  $\sigma_{nom}$  is given by Equation 7

$$K_t = \frac{\sigma_{max}}{\sigma_{nom}} = 1 + 2 \frac{a}{b} \quad (7)$$

For a hole, the stress concentration factor is classically equal to 3.

The strain concentration factor equals the stress concentration factor when no plasticity or non-linear stress-strain relations are involved.

For assessment of the feasibility to model porosity as holes in the geometry, a rectangular cavity was introduced in the coupon C1 at the location of the strain concentration shown in Figure 38. The cavity shown has a length of 0.006 inches and a width of 0.002 inches which represent approximately the dimensions and shape of the porosity void observed.

A local sub-model was built to refine the mesh around the hole as presented on Figure 39.

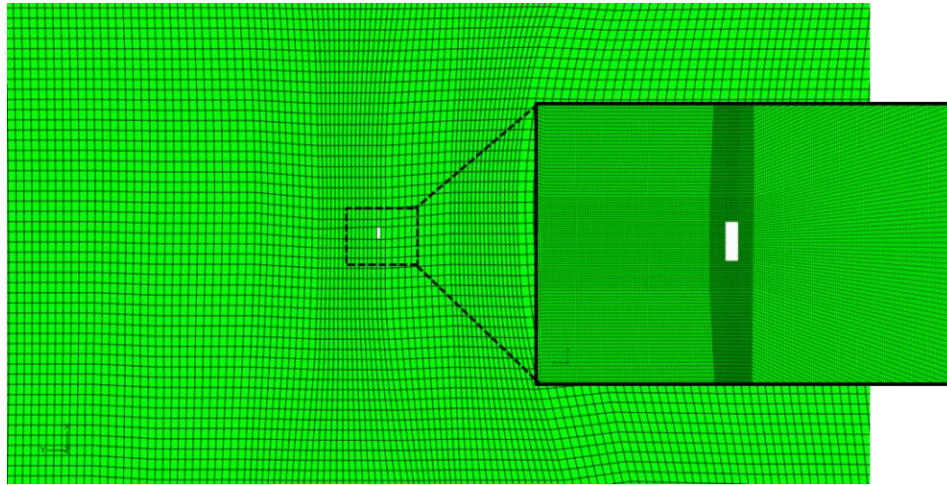


Figure 39. Global and Submodel Mesh Details for Geometry Enclosed Void.

Displacements calculated in the global model are applied as boundary conditions for the submodel. The mesh is refined around the hole to ensure a good representation of strain and stress concentrations.

Figure 42 presents the contour plot for the Interlaminar Tensile Strain at 3156lbs tensile load when a small rectangular cavity is included in the model.

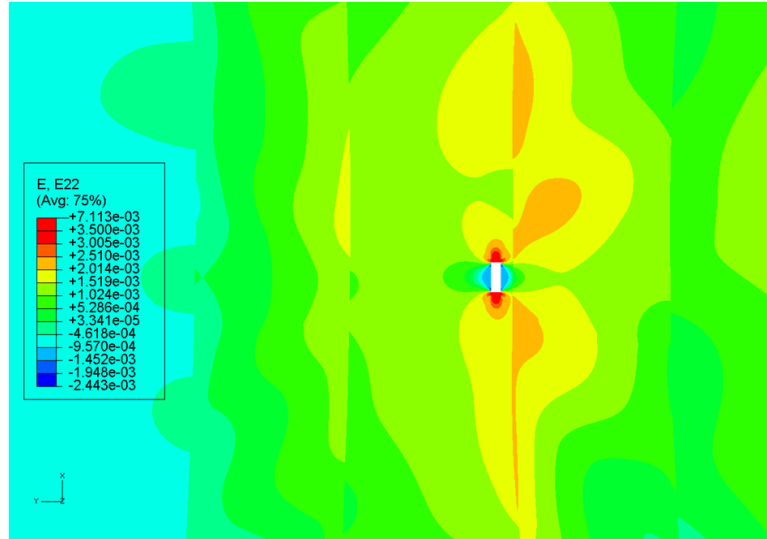


Figure 40. Interlaminar Tensile Strain for C1 at 3156lbs Tension with Rectangular Cavity.

Figure 42 shows that the inclusion of the cavity generates strain concentrations at the edges as expected. At load 3156 lbs the maximum value for interlaminar tensile strain is  $7100 \mu\epsilon$  which is about 3.2 times higher than the maximum strain level with cavity free model. However this value is still about half of the strain ( $1500 \mu\epsilon$ ) observed in the tests. The difference could be explained by the difficulty in evaluating the geometry of the void and that other phenomena such as variable resin content and local material non-linearity or local fiber buckling are probably involved.

Failure predictions based on Hashin criteria and applied to the sub-model with cavity, provided a load of 3577 lbs for failure initiation. The Interlaminar Tensile Stress criterion predicts a load of 4350 lbs.

Such loads are much lower than for previous model where no porosity defect is incorporated and closer to test results presented in Table 11. However this method appears to be limited. Exact location and shape of the voids are hard to determine. Voids can also be incorporated in the thickness and not visible from the surface. This method requires important mesh refinements around the discontinuity which can rapidly



become tedious and time consuming. A method that uses a post-processing approach by including the porosity effects in the failure criterion and does not involve modifications of geometry and mesh seems to be more appropriate.

#### **2.4.4.2 Modifying the Material Strength**

Some empirical models that take into account the effect of porosity on the strength of composite laminates have been developed in the past. Mar and Lin [18] correlated the strength of the laminate with the singularity at the crack tip. They proposed a model to express the strength  $\sigma_f$  of a laminate as a function of the diameter  $2a$  of an included circular notch :

$$\sigma_f = H(2a)^{-m} \quad (8)$$

where  $H$  is the laminate toughness and  $m$  the order of the stress singularity at the crack tip at reinforcement/matrix interface. For carbon/epoxy laminates the authors showed that the theoretical value of  $m$  is 0.28.

Almeida and Nogueira Neto [19] modified the criterion for the analysis of composite laminates containing voids using ultrasonic inspection methods assuming that:

$$\sigma_f = H(\alpha)^{-m} \quad (9)$$

where  $\alpha$  is the absorption coefficient in dB/mm of the considered laminate.

M.L. Costa and al. [20] rewrote the criterion to adapt it to a void free laminate as:

$$\sigma_f = \begin{cases} \sigma_{f0} & \text{if } \alpha \leq \alpha_{cr} \\ H(\alpha)^{-m} & \text{if } \alpha > \alpha_{cr} \end{cases} \quad (10)$$

Where  $\sigma_{f0}$  is the fracture stress of a void free laminate and  $\alpha_{cr}$  is the critical value of the absorption coefficient given by:

$$\alpha_{cr} = \left( \frac{\sigma_{f0}}{H} \right)^{-\frac{1}{m}} \quad (11)$$

Such models showed good correlations with test data using 3 points bending tests [20] to evaluate Interlaminar Tensile and Shear Strength.

An interesting effort would be to take into account this modification of strength properties in finite element models for the small coupons. This would consist in a simple modification in the definition of damage indexes in the subroutine. However this requires specific tests data to determine the absorption coefficient  $\alpha$  for each coupons. Such data were not available in the framework of this thesis but could be the objective of the follow-up effort.

## **CHAPTER 3: Failure Prediction for Open Hole Carbon/epoxy Laminate**

### **3.1 Problem Presentation**

The presence of circular holes in composite laminates is common for composite applications in the aerospace structures. Indeed, mechanical fasteners and rivet holes are used for various attachments. Holes in composite structures will result in local stress concentrations that will reduce the structural strength. The failure will depend strongly on the lay-up and the stacking sequence of considered laminates. The objective is to assess the capability of prediction for matrix-dominated failure onset and propagation in multi-directional lay-up carbon/epoxy laminates in presence of an open hole. FEM prediction will be compared to test data for laminates under tensile load.

The specimen selected is a  $[45/0/-45/90]_{2S}$  carbon/epoxy IM7/8552 tape open-hole coupon. The coupon width is 1.5 inches and untabbed length is 7.5 inches, thickness is 0.104 inches and a 0.25 inch-diameter hole is drilled.

The specimen was submitted to tensile load and strains were monitored using the VIC technique. X-Rays pictures were taken during loading to detect the formation of cracks under the surface. Figure 41 shows the presence of matrix cracking in both 90 deg. and 45 deg. plies at ultimate failure.

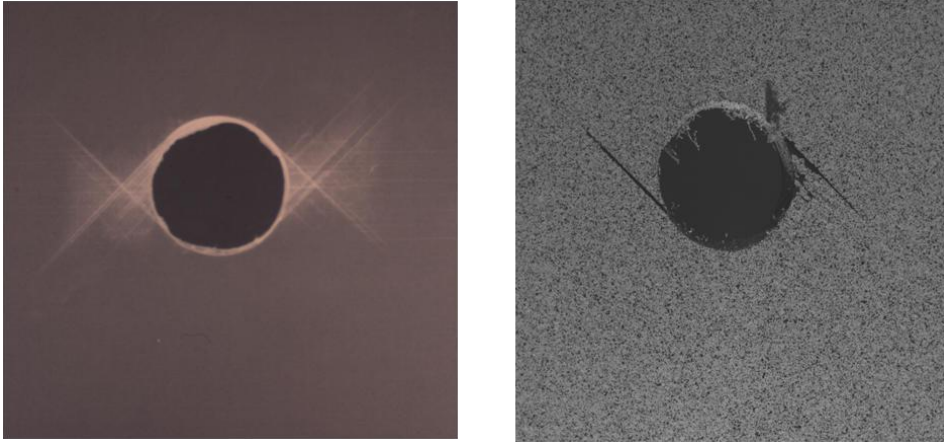


Figure 41. Subsurface (X-Ray) and Surface (DIC) Images just before Ultimate Failure

Tests revealed that matrix cracking starts to occur in 90 deg. plies around 4000 lbs tensile load. As the load increases, new cracks in 90 deg. plies start and propagate and first cracks in 45 deg appear around 5000 lbs. Ultimate Failure occurs by unstable opening of the 45 deg plies at 8000 lbs as shown in the Figure above.

## **3.2 ABAQUS Finite Element Model**

### **3.2.1 3D Finite Element Mesh**

A 3D finite element model of the coupon is built using 3D stress 8 nodes elements C3D8R.

Since a 3D model involves large number of Degrees of Freedom, a sub-modeling technique is used to refine locally the mesh around the hole. Figure 42 presents the global and sub-model meshes generated for the open-hole coupon.

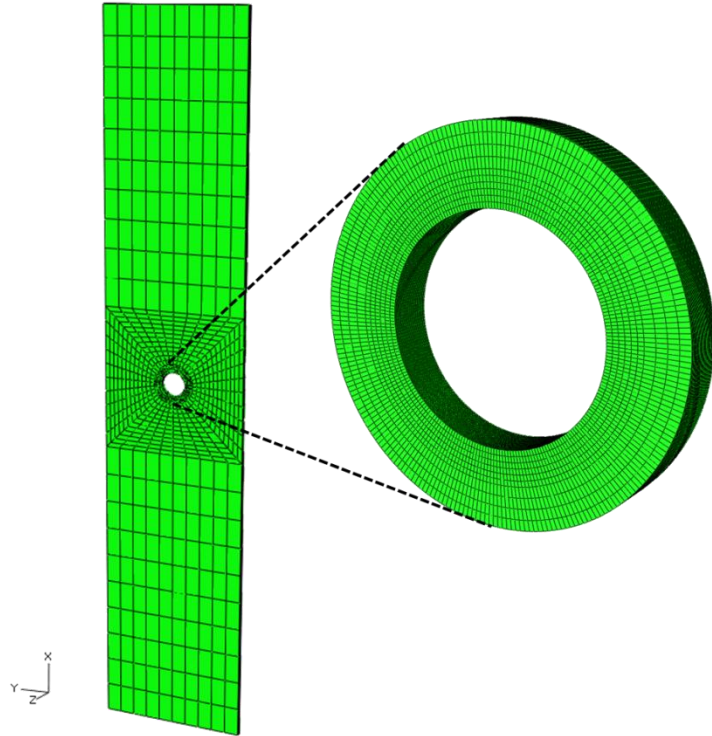


Figure 42. Global and Sub-model 3D Finite Element Model for Open Hole Coupon

ABAQUS node-based sub-modeling technique is used so that the sub-model is driven at its boundaries by nodal results for displacements calculated for the global model.

Since the  $[45/0/-45/90]_2S$  lay-up is symmetric, Z-symmetry boundary conditions are applied to one face of the model to reduce the number of degree of freedom. Boundary fixed displacements are applied at the lower end and uniform axial displacements with applied tensile force at the upper end.

Material properties for carbon/epoxy material IM7/8552 listed on Table 4 are assigned to the ply layers with orientations defined according to the stacking sequence. Non-linear stress-strain models for interlaminar shear properties developed in 2.3.1.2 and illustrated in Figure 10 are implemented.

### 3.2.2 Mesh Convergence

The problem of mesh convergence is addressed to ensure a correct representation of stress concentrations around the hole. Convergence study is conducted only on the sub-model since the large stresses gradients involved are located around the hole. The sub-model ring is partitioned in eight regions. Figure 43 shows the four mesh seed parameters for the mesh generation: a determines the number of elements on the circumference, and b and c characterize the radial density of elements and t the number of elements through the thickness.

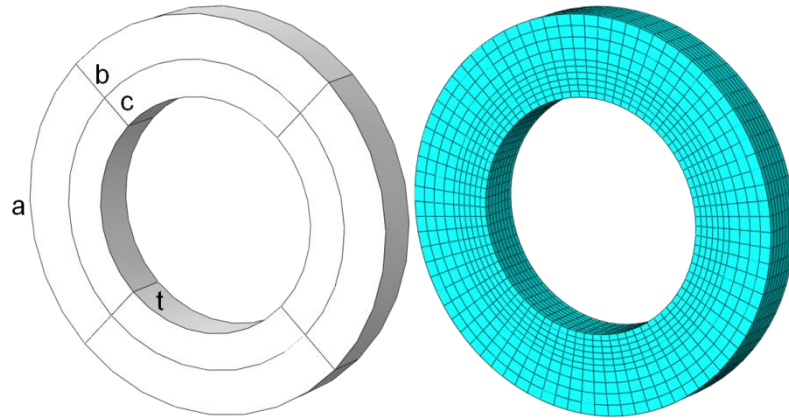


Figure 43. Mesh Seed Parameters for Mesh Convergence Study

No damage model is included in the convergence study but non-linear properties for interlaminar shear are implemented. An arbitrary tensile load of 1854 lbs (8250 N) is applied to the global model that drives the sub-model.

The different stresses expressed in global coordinate system are considered. The influence of each mesh seed parameter is evaluated separately.

Since stresses gradients are located at the hole edges and mainly in the interior ring, convergence is quickly achieved for parameter b. Table 12 compares the maximum values of the different stresses with 4 and 8 elements for mesh seed parameter b.

Table 12. Influence of Parameter b in Mesh Convergence for Maximum Stresses

<b>b</b> (nb of elements)	<b>4</b>	<b>8</b>
<b>S11</b> (MPa)	1368	1368
<b>S22</b> (MPa)	302.4	301.4
<b>S33</b> (MPa)	25.10	25.01
<b>S12</b> (MPa)	335.6	335.6
<b>S13</b> (MPa)	38.90	38.92
<b>S23</b> (MPa)	21.35	21.34

As shown in Table 12, results with 8 elements differ to results with 4 elements by less than 0.4% of maximal error for  $S_{22}$  and thus convergence is established with 4 elements.

To determine the required number of elements for parameters a, c and t, Interlaminar Stresses  $S_{22}$ ,  $S_{12}$  and  $S_{33}$  are examined along a path through the thickness, as illustrated on Figure 44 for  $S_{22}$ . Maximum values for the considered stress are located on the path defined as illustrated.

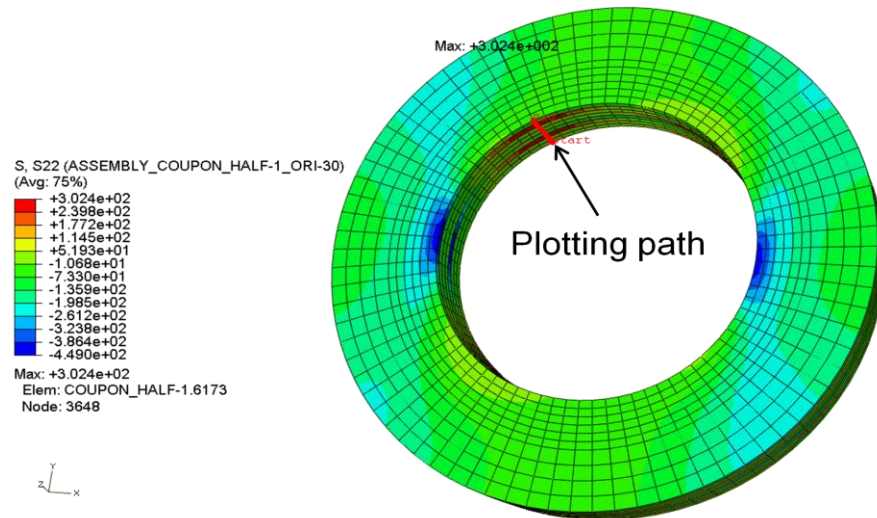


Figure 44. Stresses Plotting Path for Mesh Convergence Study

Figure 45 - Figure 53 present the influence of the different seeding parameter on the convergence for  $S_{22}$ ,  $S_{12}$  and  $S_{33}$

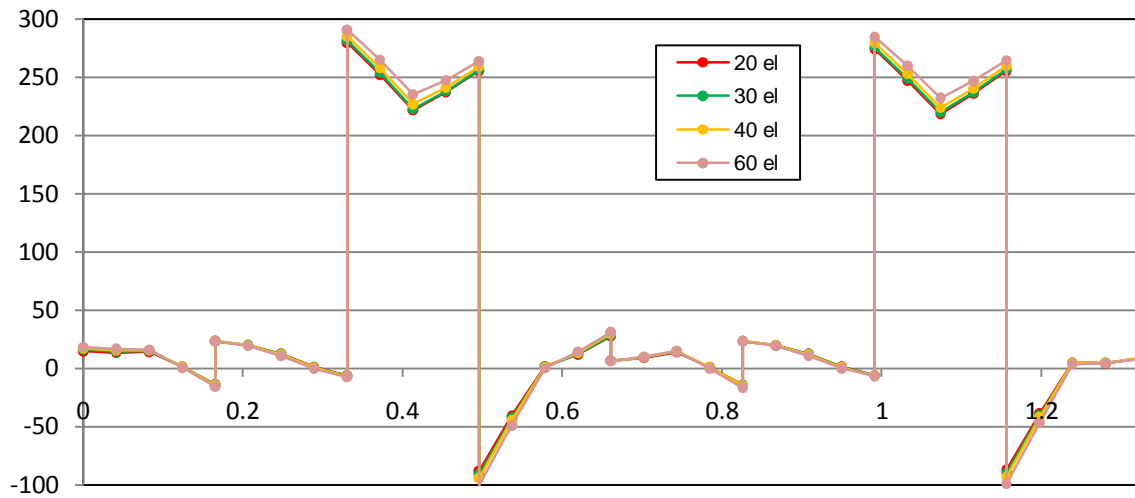


Figure 45. Influence of Circumferential Parameter  $a$  for  $S_{22}$  Convergence

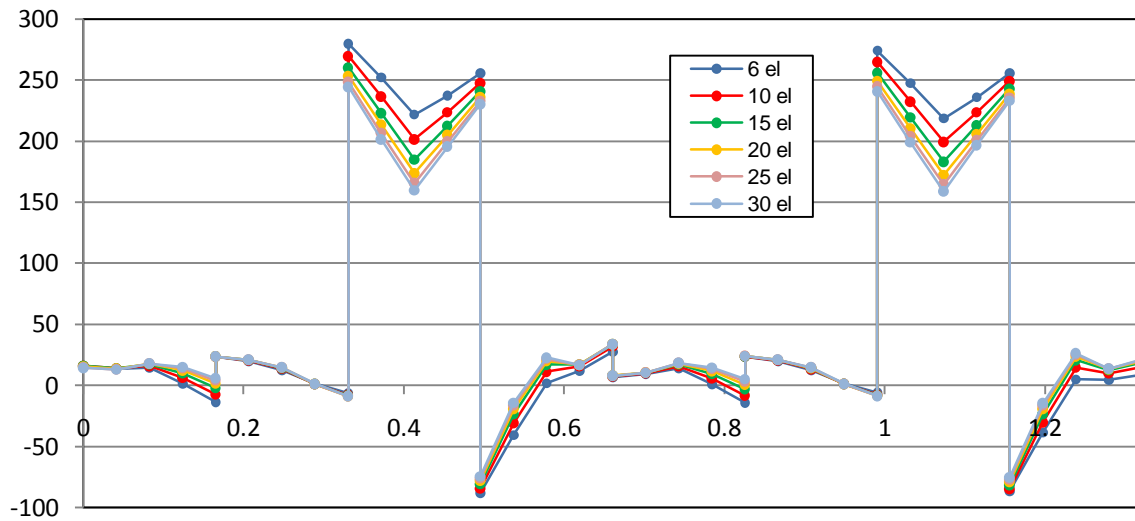


Figure 46. Influence of Radial Parameter  $c$  for  $S_{22}$  Convergence



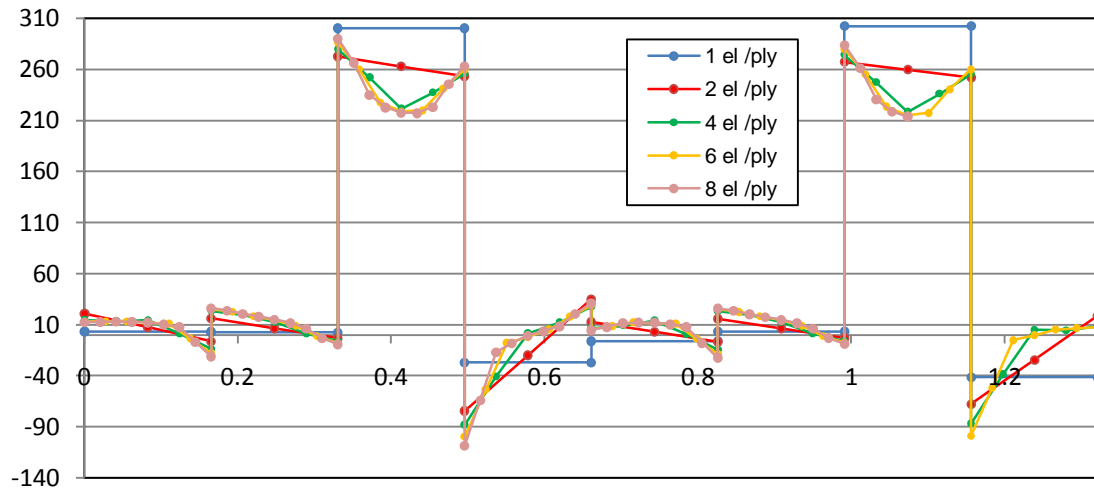


Figure 47. Influence of Through-thickness Parameter  $t$  for  $S_{22}$  Convergence

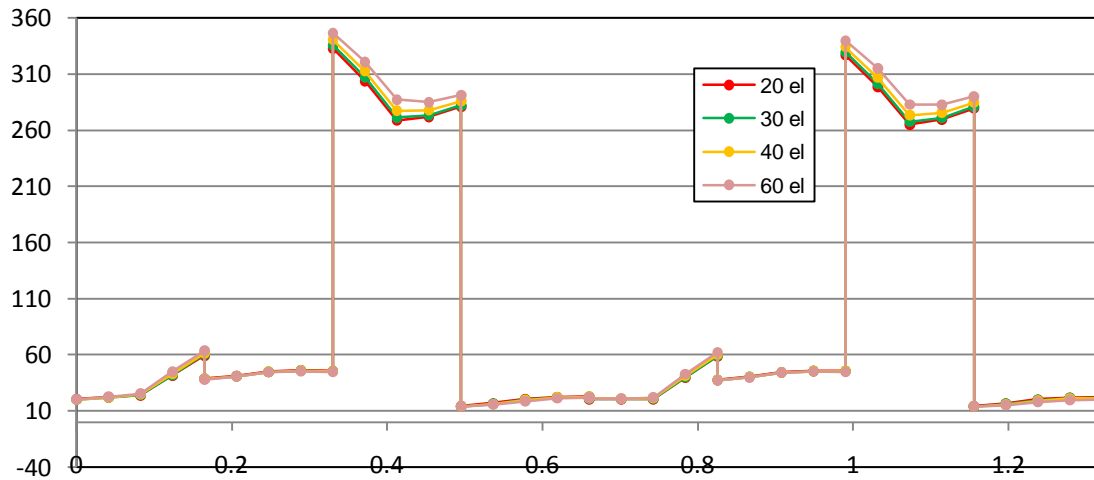


Figure 48. Influence of Circumferential Parameter  $a$  for  $S_{12}$  Convergence

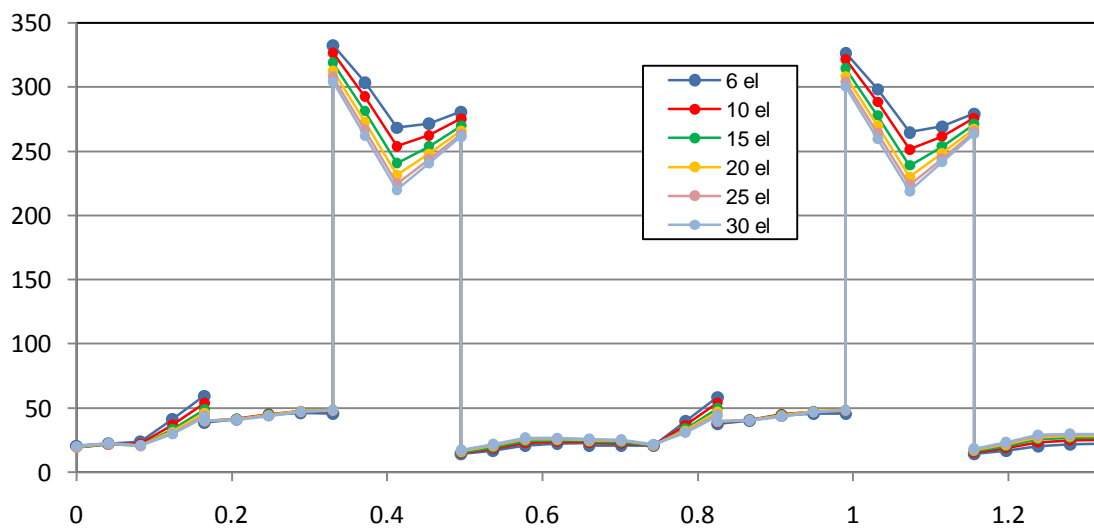


Figure 49. Influence of Radial Parameter  $c$  for  $S_{12}$  Convergence

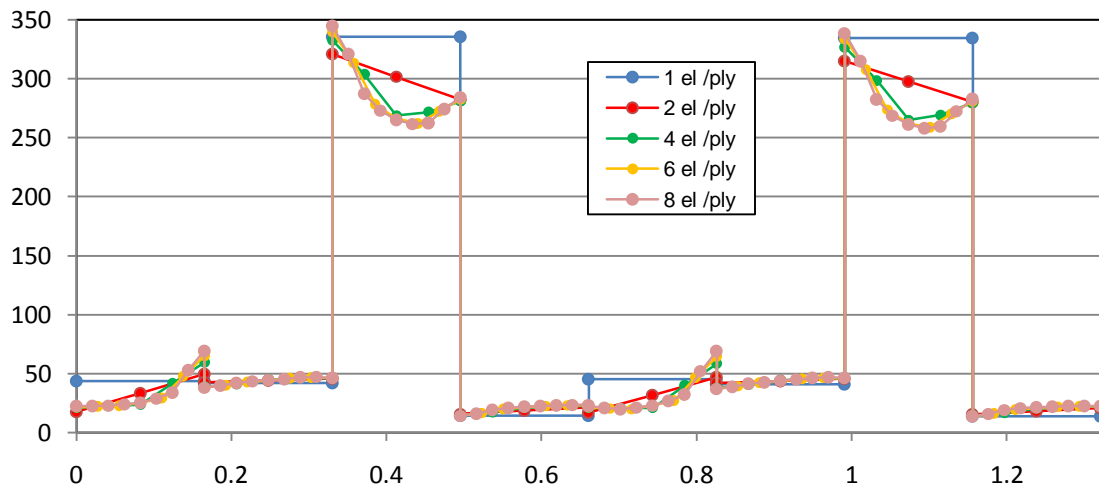


Figure 50. Influence of Through-thickness Parameter  $t$  for  $S_{12}$  Convergence

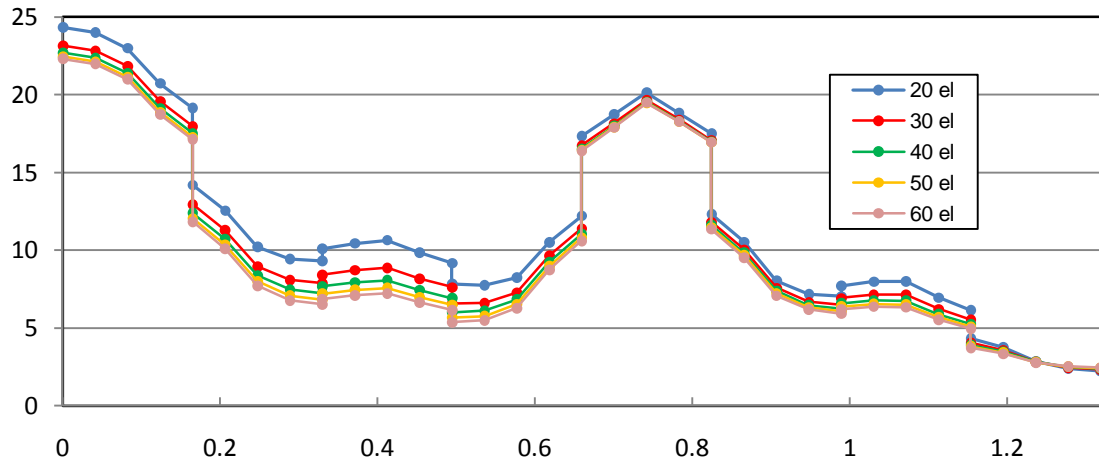


Figure 51. Influence of Circumferential Parameter  $a$  for  $S_{33}$  Convergence

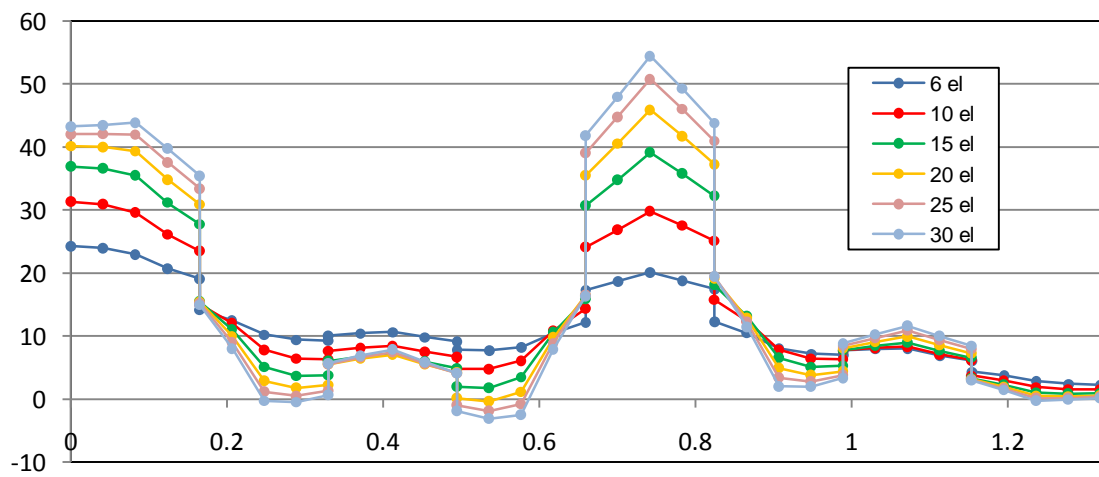


Figure 52. Influence of Radial Parameter  $c$  for  $S_{33}$  Convergence

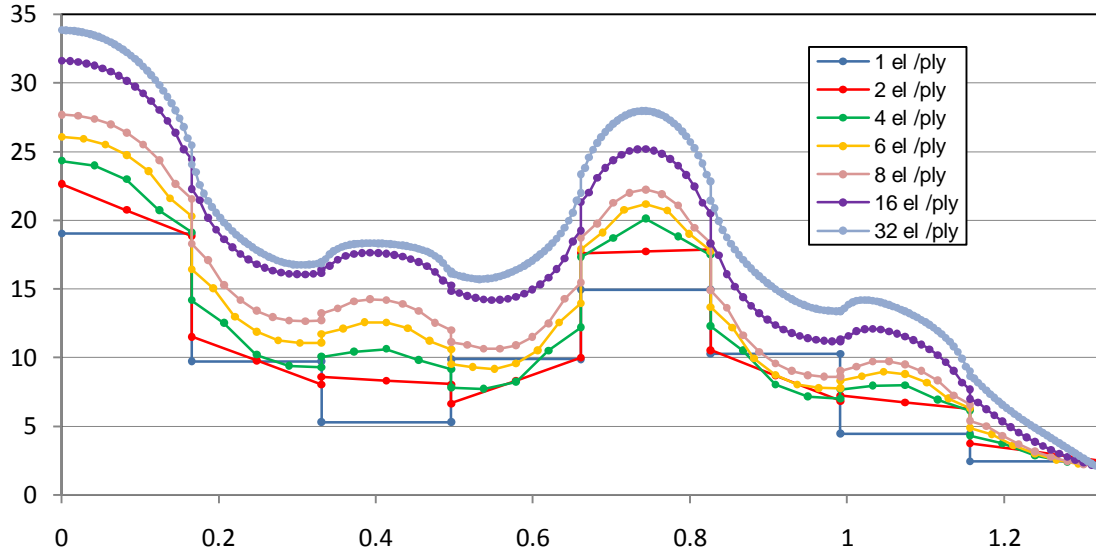


Figure 53. Influence of Through-thickness Parameter  $t$  for  $S_{33}$  Convergence

Figure 45, Figure 48, and Figure 51 show that convergence is quickly achieved for the circumferential mesh seed parameter  $a$  (number of elements per quarter circumference). The three stresses reach acceptable convergence with 40 elements.

Figure 46 and Figure 52 show that a fine mesh in the radial direction around the hole is necessary to calculate accurately interlaminar stresses  $S_{22}$  and  $S_{33}$  (convergence is quickly reached for  $S_{12}$ ). 25 elements for mesh seed parameter  $c$  allow to reach convergence for  $S_{22}$ . However more than 30 elements are required to reach convergence for  $S_{33}$  as shown in Figure 52.

Figure 47, Figure 50, and Figure 53 show the influence of the number of elements per ply (through the thickness) in stress convergence. The results for stresses  $S_{22}$  and  $S_{12}$  show that satisfactory convergence is reached when 4 elements per plies are assigned. Figure 53 shows that for  $S_{33}$  even 32 elements per plies are not enough for the results to converge. Such a refinement through the thickness results already in a very large sub-model with more than 680,000 DOF and leads to the conclusion that convergence does not seem to be reasonably reachable for interlaminar stress  $S_{33}$ .

To summarize, the mesh convergence study showed that 40 elements for mesh seed a, 6 elements for mesh seed b, 25 elements for mesh seed c and 4 elements per ply-thickness ensure accurate results for interlaminar tensile and shear stresses  $S_{22}$  and  $S_{12}$ .

The study also demonstrated that the finite element models developed are not able to solve the problem for transverse stress  $S_{33}$  within the available computational capacity.

This incapacity comes from the fact that the finite element models does not take into account the changes in the micro-structure between two layers. Stiffness properties brutally change between two group of plies which is a mathematical description and not a meaningful representation of physical reality. De Borst [21] proposed numerical corrections by introducing additional terms in continuum description to address this problem. These corrections where not considered in the framework of this thesis. Regarding failure predictions, the incapacity to have an accurate  $S_{33}$  representation means that the effects of out of plane stress components should not be included in the damage model. However this should not interfere too much on the accuracy of predictions, since matrix cracking is expected to occur mainly because of in plane stress and shear concentrations. This is confirmed by the fact that maximum stress values simulated for  $S_{22}$  and  $S_{12}$  are about 7 times higher than the maximum value for  $S_{33}$ .

### **3.2.3 Failure Model**

#### ***3.2.3.1 Damage Initiation Criterion***

To predict the initiation of matrix cracking in the laminate, a criterion that takes into account the combined effect of in-plane transverse tension and shear is necessary. P. Camanho *et al.* [22] showed that a criterion based on fracture mechanics models of cracks in laminates leads to good correlation with experimental results. The criterion

they used is based on the Hahn [23] mixed mode criterion written as a polynomial in the stress intensity factors  $K_I$  and  $K_{II}$  at the tip of the crack:

$$(1 - g) \frac{K_I}{K_{Ic}} + g \left( \frac{K_I}{K_{Ic}} \right)^2 + \left( \frac{K_{II}}{K_{IIc}} \right)^2 \leq 1 \quad (12)$$

with  $g = \frac{G_{Ic}}{G_{IIc}}$  where  $G_{Ic}$  and  $G_{IIc}$  are the fracture toughness (critical energy release rate) for mode I (tension) and mode II (shear) fracture.  $K_{Ic}$  and  $K_{IIc}$  are the critical stress intensity factors.

Using Fracture Mechanics for a slit crack, the authors showed that the criteria for linear shear stress-strain response can be expressed in term of stresses and strength as a damage index  $D$  :

$$D = (1 - g) \frac{\sigma_{22}}{S_{22}} + g \left( \frac{\sigma_{22}}{S_{22}} \right)^2 + \left( \frac{\sigma_{12}}{S_{12}} \right)^2 \leq 1 \quad (13)$$

where  $S_{22}$  and  $S_{12}$  are the interlaminar tensile and shear strength.

For non-linear shear behavior the last term of the criterion must be modified. Camanho and al. [22] proposed to use the Sandhu [24] assumption for failure prediction in non-linear materials using the contribution of shear stress and shear strain to the strain energy density as :

$$D = (1 - g) \frac{\sigma_{22}}{S_{22}} + g \left( \frac{\sigma_{22}}{S_{22}} \right)^2 + \frac{\chi(\gamma_{12})}{\chi(\gamma_{12}^u)} \leq 1 \quad (14)$$

where  $\gamma_{12}^u$  is the maximum admissible shear strain defined using Equation 1 as :

$$\gamma_{12}^u = \frac{S_{12}}{G_{12}} + \left( \frac{S_{12}}{K} \right)^{\frac{1}{n}} \quad (15)$$

The strain density  $\chi(\gamma_{12})$  can be determined analytically knowing the non-linear shear behavior  $\sigma_{12} = \sigma_{12}(\gamma_{12})$  and is defined as:

$$\chi(\gamma_{12}) = 2 \int_0^{\gamma_{12}} \sigma_{12} d\gamma_{12} \quad (16)$$

Using the relation given by Equation 3 extrapolated from test data, we can integrate that relation in :

$$\chi(\gamma_{12}) = 2 \left( G_{12} \frac{\gamma_{12}^2}{2} + a \frac{\gamma_{12}^3}{3} + b \frac{\gamma_{12}^4}{4} + c \frac{\gamma_{12}^5}{5} + d \frac{\gamma_{12}^6}{6} \right) \quad (17)$$

We can point out that P. Camanho and al. [22] recommended to use what they call 'in-situ' strength rather than the unidirectional strength properties, assessing that transverse tensile and shear strengths are higher when a ply is constrained by plies with different fiber orientations in a laminate. Strength also depends on the number of plies embedded together. The corrected strength properties listed in Table 4 take into account that consideration.

The assumption that compressive stress do not contribute to damage is also done and the damage criterion [22] given by Equation 14 is finally expressed as :

$$D = \begin{cases} (1 - g) \frac{\sigma_{22}}{S_{22}} + g \left( \frac{\sigma_{22}}{S_{22}} \right)^2 + \frac{\chi(\gamma_{12})}{\chi(\gamma_{12}^u)} & \text{if } \sigma_{22} \geq 0 \\ \frac{\chi(\gamma_{12})}{\chi(\gamma_{12}^u)} & \text{if } \sigma_{22} < 0 \end{cases} \quad (18)$$

### 3.2.3.2 Damage Propagation

To simulate damage propagation of matrix cracking a damage model with stiffness softening needs to be implemented in finite element models. A simple approach consists in considering that once the damage onset variable  $D$  is saturated for one element, stiffness properties in the directions of failure modes involved are dropped to zero. Thus, for matrix cracking where in plane interlaminar tensile stress and shear stress contributions are taken into account, damage propagation is insured by dropping the transverse and shear stiffness properties to zero.

The described damage pattern is introduced in finite element model by using the ABAQUS user subroutine USDFLD [16] used previously to introduce non-linear material properties for shear. A field variable  $FV$  is defined as followed :

$$FV = \begin{cases} 1 & \text{if } D \geq 1 \\ 0 & \text{otherwise} \end{cases} \quad (19)$$

The dependence of material properties on field variable FV is described by Table 13:

Table 13. Dependencies on Damage Field Variables for Matrix Cracking

Material State	Material properties									Field variable FV
No failure	E <sub>11</sub>	E <sub>22</sub>	E <sub>33</sub>	v <sub>12</sub>	v <sub>13</sub>	v <sub>23</sub>	G <sub>12</sub>	G <sub>13</sub>	G <sub>23</sub>	0
Matrix failure	E <sub>11</sub>	0	0	0	0	0	0	0	0	1

To be accurate, this method requires a small time increment since the damage onset variable D is evaluated from stress and strain state at the previous increment. The advantage of that method is that it is free of convergence problems that can occur when element stiffness is brutally dropped to zero. Such problems can be encountered for example when ABAQUS subroutine UMAT [16] is used to introduce the stiffness softening in the stress-strain relation.

### 3.3 Finite Element Analysis Results and Test Comparison

#### 3.3.1 Fiber Oriented Finite Element Mesh

A global mesh and sub-model meshes are generated using necessary mesh refinements determined by previous convergence study.

The mesh was generated as presented on Figure 42 with radially-oriented elements around the hole. A preliminary analysis showed that results were dependent of the elements orientation. Figure 54 presents the contour plot for damage variable D at a 6240 lbs tensile load.

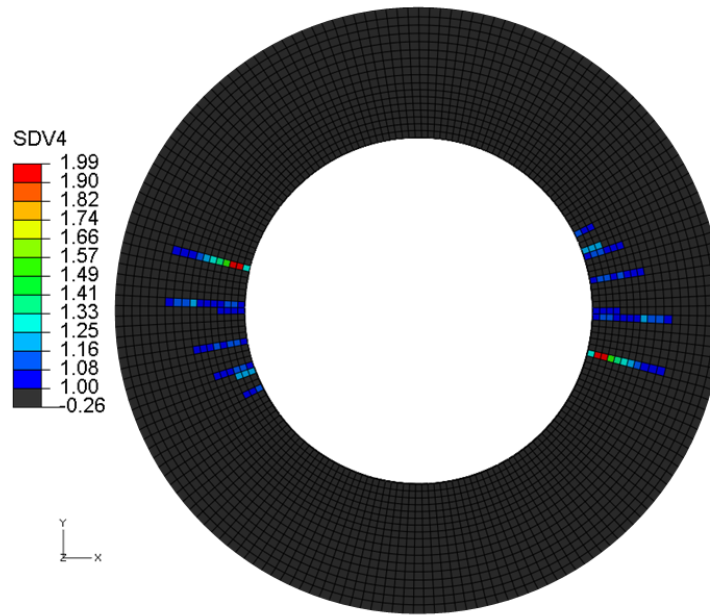


Figure 54. Damage Contour plot at 6240lbs for 90 deg surface ply

Figure 54 highlights the development of cracks in the surface 90 deg. ply. The location of cracks initiation sites at which they first occur is consistent with test results. However the direction of propagation for the cracks seems to be determined by the orientation of elements. Matrix-cracks in the 90 deg. plies are supposed to occur along the fiber direction and perpendicularly to the loading axis and not as shown. The same observation can be done for cracks developments in 45 deg. plies. This questions the validity of the model since local equilibriums of the structure are modified by cracks developments and failure load predictions become inaccurate. This dependence in element orientations and aspect ratio has been mentioned by researchers such as De Borst and Remmers [21].

ABAQUS CAE is unable to produce a structured mesh with fixed elements orientation in the presence of a hole. To address this problem, a mesh with fiber oriented elements has been developed at Georgia Institute of Technology by Senior Research Engineer



Yuri Nikishkov using a C++ code. Figure 55 presents the fiber oriented final mesh generated for the sub-model.

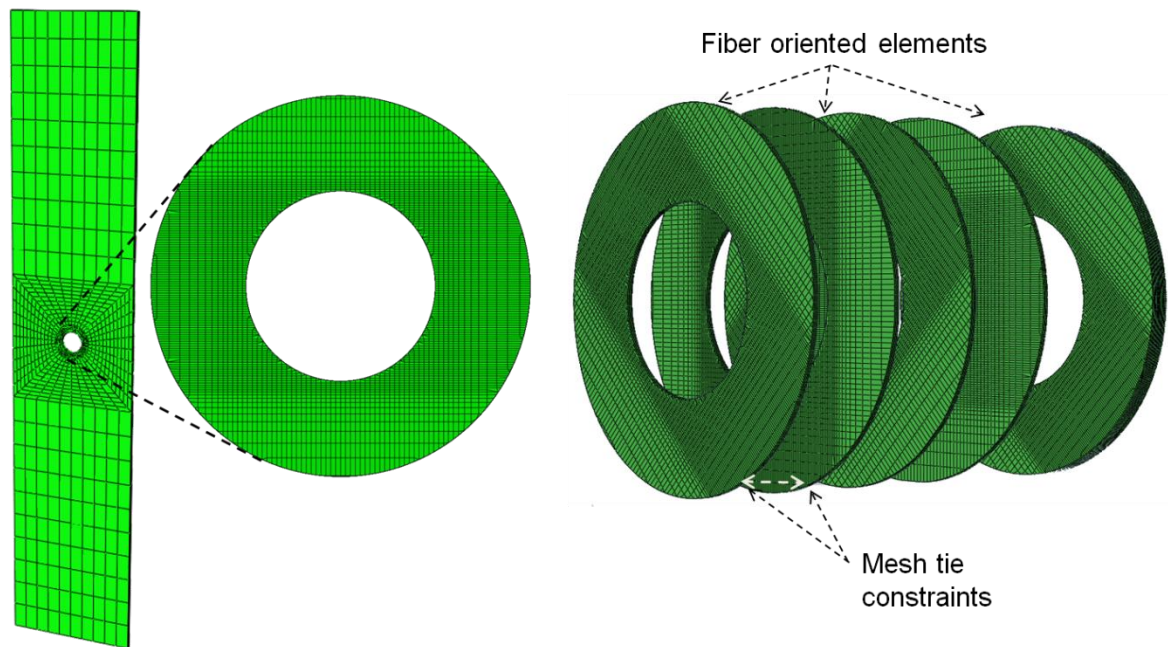


Figure 55. Global and Sub-model Meshes for Open Hole Coupon Analysis

As shown in Figure 55, elements are oriented along fiber direction for each group of plies. Surface-based tie constraints are defined between the plies to tie together the unmatched section meshes. Mesh is refined with seed biases around the hole.

A coarse mesh with one element per ply and 33,240 DOF is used for the global model. No damage model is implemented for the global model analysis, but non-linear shear material properties are incorporated. The sub-model includes 4 elements per ply and about 500,000 DOF. Damage initiation and propagation models developed for matrix cracking in paragraph 3.2.3 are included.

A load of 11915 lbs (530000N) is applied to the global model. That load is applied in 2 steps. A first step with 50 increments is defined to go to 3710 lbs (16500N) tensile load where no damage should have occurred according to tests results. The second step

takes 365 increments defined to apply a final load of 11915 lbs (530000N) by increasing the global load of 100N at each increment.

### 3.3.2 Finite Element Analysis Results and Test Data Comparison

#### 3.3.2.1 Matrix Cracking Initiation and Propagation

Damage variable D is plotted to detect matrix-crack initiation and to observe its propagation when applied tensile load is increased. Figure 56 - Figure 59 present the damage variable contour plot for different load levels.

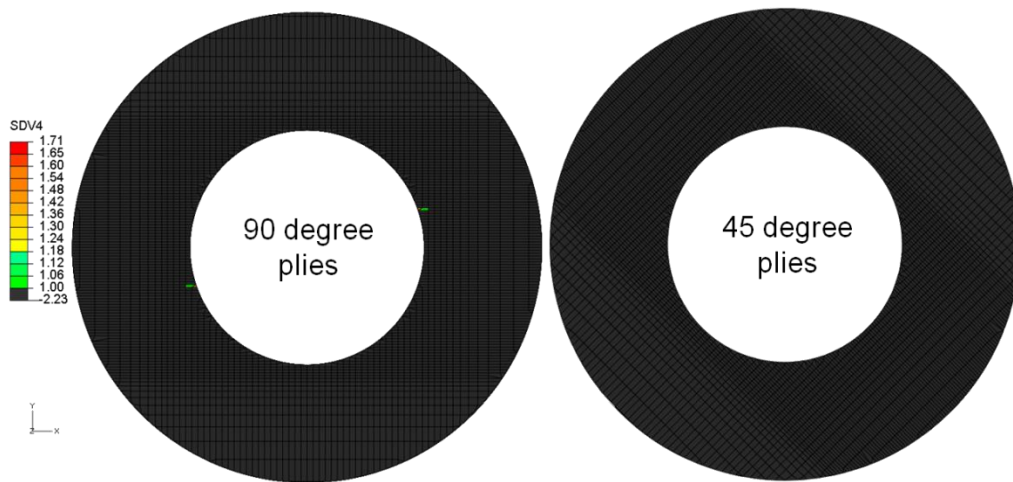


Figure 56. Damage Plot for Open-Hole Coupon at 4226 lbs Tension

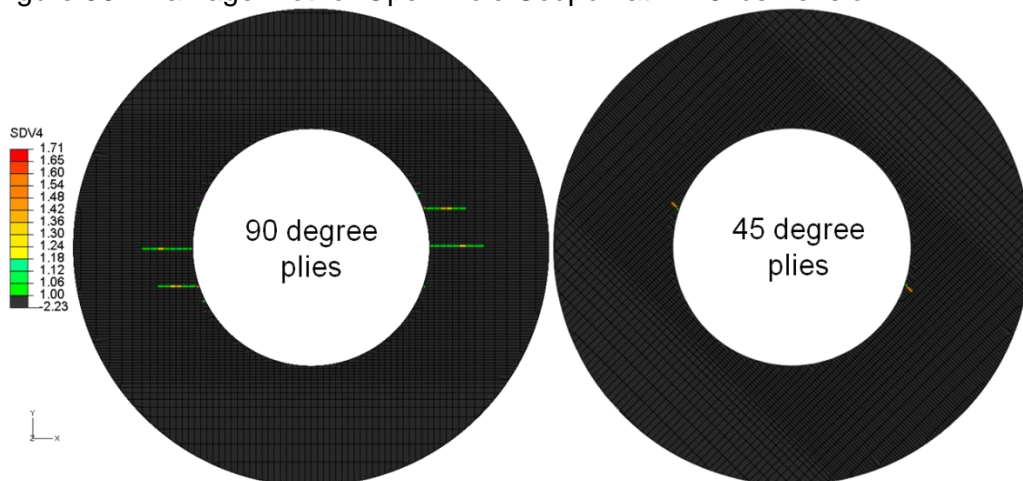


Figure 57. Damage Plot for Open-Hole Coupon at 4991 lbs Tension

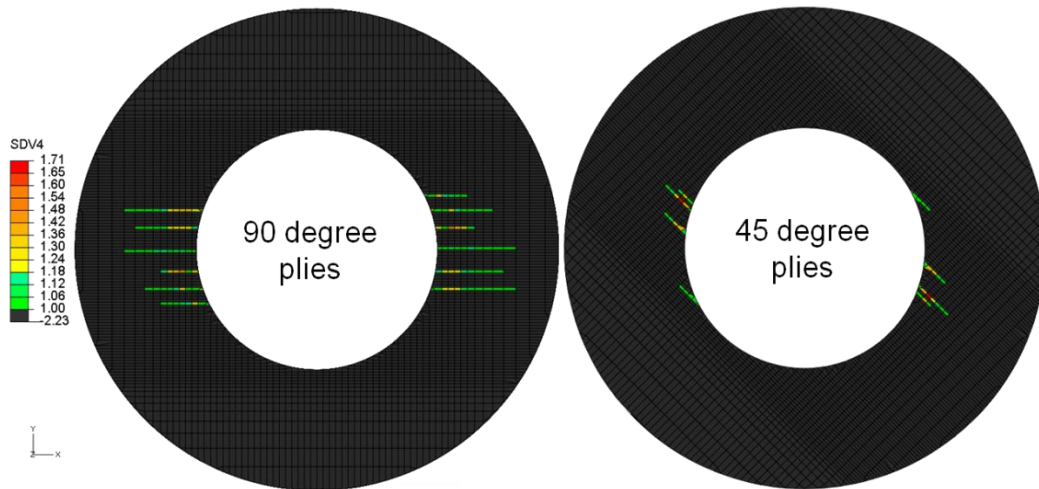


Figure 58. Damage Plot for Open Hole Coupon at 5953 lbs Tension

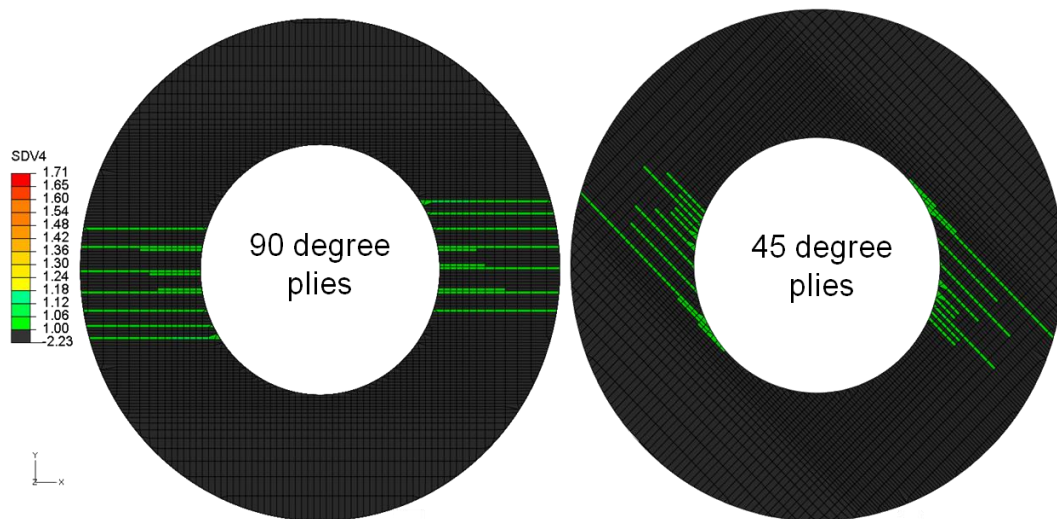


Figure 59. Damage Plot for Open Hole Coupon at 8475 lbs Tension

Figure 56 - Figure 59 show the predicted development of matrix cracking in the 90 deg. and 45 deg. plies. The first crack initiates at 4226 lbs tension in the 90 deg. plies as shown in Figure 56. At that first stage no damage has already occurred in the 45 deg. plies. Cracks in the 90-degree plies will continue to initiate and propagate until they reach the boundary of the sub-model. Cracks develop anti-symmetrically on each side of the hole.

The first crack in 45 deg. plies occurs at 5032 lbs as illustrated in Figure 57. More cracks keep on developing in 45 deg. plies as the load increases but their propagations stop. At

7239 lbs a new crack starts to develop in the 45 deg. plies on each side of the hole, initiating at about 45 deg. and 225 deg. radial positions. This crack will not stop as the load increases and will propagate quickly until it reaches the sub-model model boundary at 8475lbs. This corresponds to the ultimate failure of the structure. Figure 60 compares the FEM results with ultimate crack and a picture of the test sample after ultimate failure has occurred.

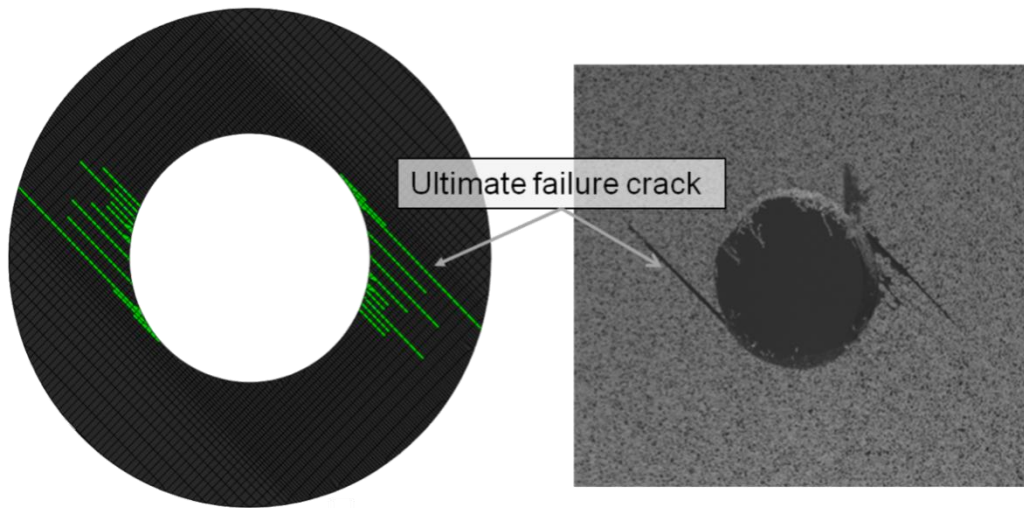


Figure 60. Ultimate Failure Crack for Open Hole Coupon.

### **3.3.2.2 Test Data Correlation**

Strains predicted by the FEM are compared to tests data as presented on Figure 61 - Figure 64.



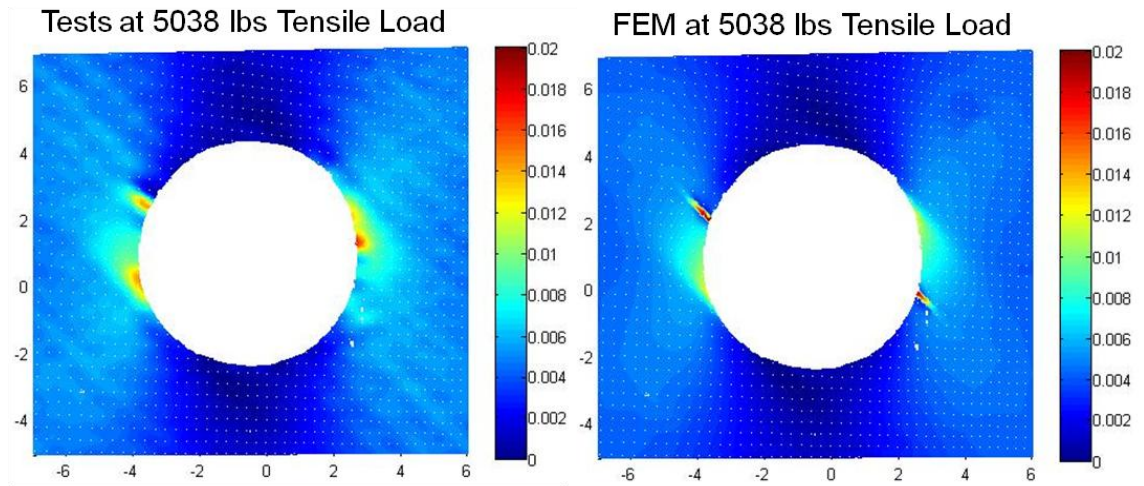


Figure 61. Surface Transverse Strain Correlation at 1st 45 deg. Crack Development

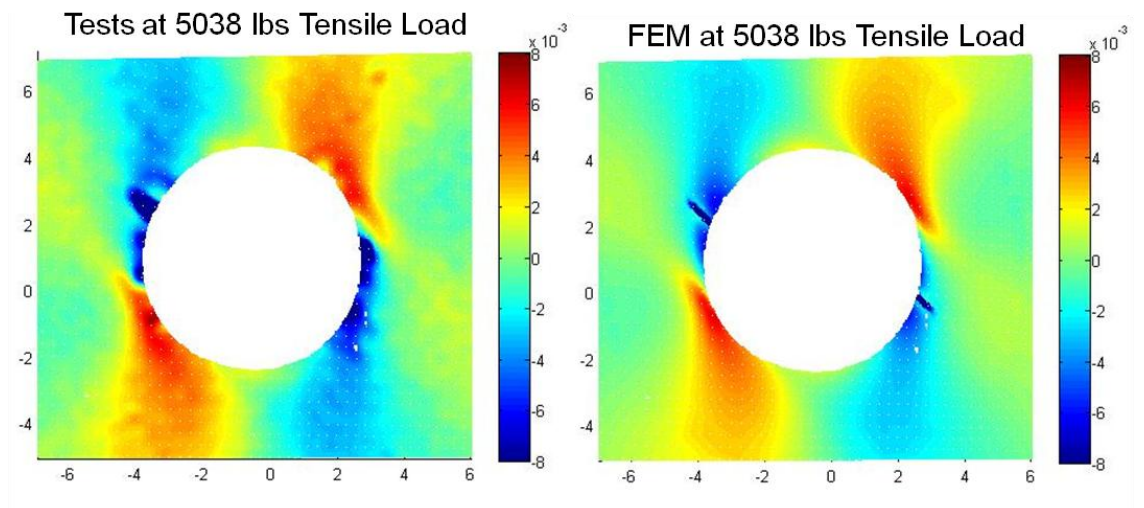


Figure 62. Surface Shear Strain Correlation at 1st 45 deg. Crack Development

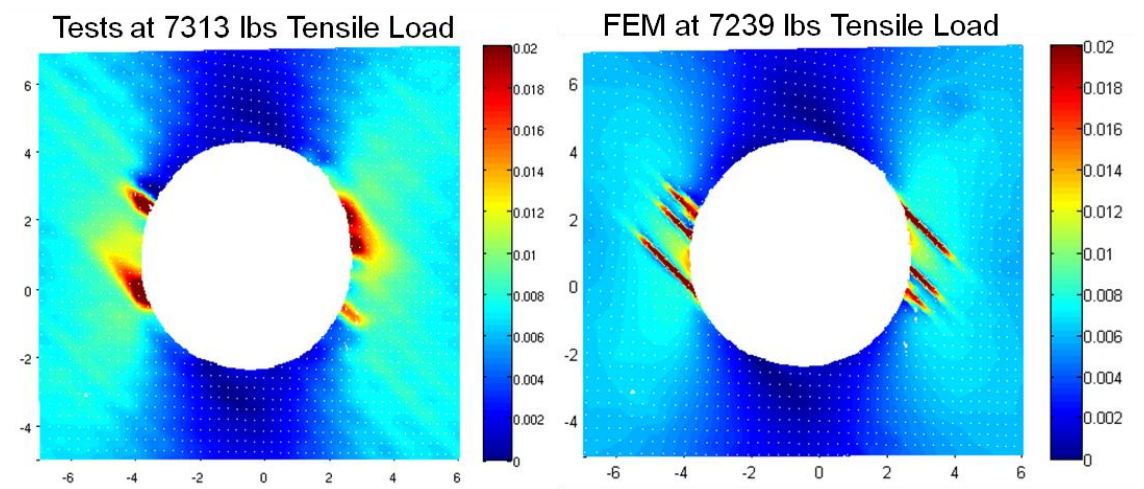


Figure 63. Surface Transverse Strain Correlation at Ultimate Crack Development

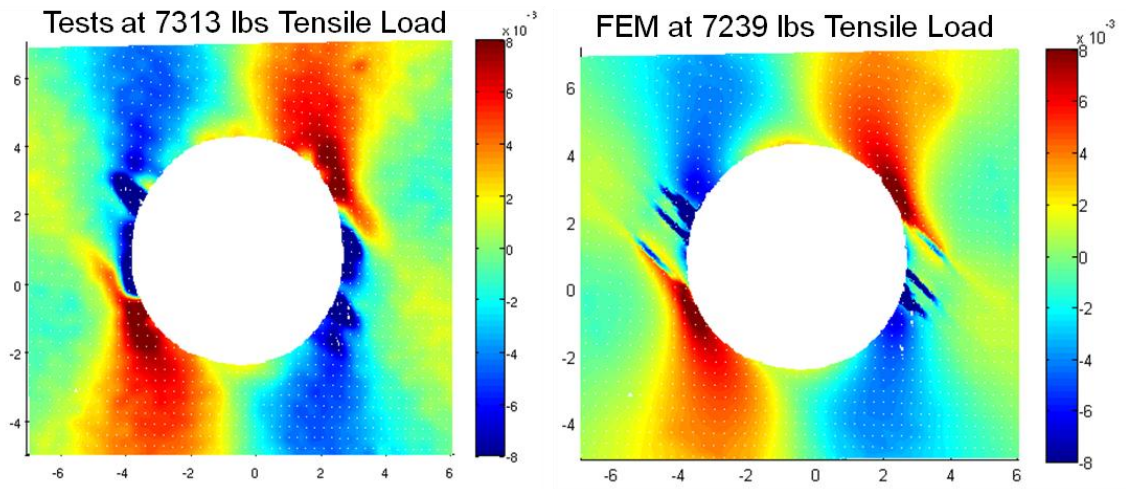


Figure 64. Surface Shear Strain Correlation at Ultimate Crack Development

FEM predictions are in agreement with tests results for interlaminar tensile and shear strains. On Figure 63 and Figure 64 some slight differences can be observed between FEM in the number and location of cracks on each side of the hole. These differences are probably due to effects of unmodeled macroscopic imperfections of the structure. But failure models developed exhibit a good capability to predict accurately the location of cracks initiation as well as their sequence of apparition. Table 14 summarizes the predicted and tested loads for different cracks developments.

Table 14. Summary of Predictions and Test Data for Hole Coupon

Crack developments	Test data	FEM
$\pm 45$ -deg. ply cracking	5038 lbs	4991 lbs
Development of ultimate crack	7313 lbs	7284 lbs
Ultimate Failure	8361 lbs	8475 lbs

Predictions and Tests are in very good agreement and the failure models developed for matrix cracking are validated for future utilization in prediction initiation and ultimate failure by matrix cracking in thick carbon/epoxy laminates.

This effort could be continued by further developments of failure models. Almost vertical stiffness softening law is can be improved by taking into the energy released during the cracks and use models for damage propagation developed for cohesive zone models [21]. The problem of delamination combined to matrix cracking could also be addressed by refining damage models at layers interfaces or by including cohesive zone models[25],[26][27] .

## CHAPTER 4: CONCLUSION

Finite element-based interlaminar failure models were developed for IM7/8552 Carbon/Epoxy tape laminate with wavy plies. Strength of material approach is accurate for predictions of the onset of delamination. A mixed-mode Hashin failure criterion is in agreement with test data (DIC). This work also shows the importance of implementing nonlinear interlaminar shear stress-strain relations in the failure models of carbon/epoxy tape composites. The presence of porosity voids in test specimens with small wrinkles showed that such manufacturing defect could influence drastically the structural strength behavior. Models for porosity must be included in finite element models when its presence becomes evident. A suitable approach could be the definition of failure criteria taking into account porosity once it has been quantified in the laminate.

It is worth noting that for the wrinkle Carbon/Epoxy coupons, delamination propagation occurred quasi instantaneously after the first crack was initiated. Hence modeling damage propagation was not necessary. But composite structures can exhibit significant residual strength after initiation and modeling damage propagation is important. Stress-based and fracture mechanics-based failure models using 3D solid elements were implemented to model the onset and multi-step propagation of In-ply matrix cracking in open hole carbon/epoxy laminates. Convergence study showed the importance of the mesh definition to address properly the problem. A submodeling technique was used to refine locally the number of elements in order to simulate accurately stresses concentrations around the hole. The development of a fiber-oriented mesh was necessary to model correctly the propagation of cracks. Very good agreement with test data were documented for prediction of crack initiation and ultimate failure. Failure models could be improved by including fracture mechanics-based models for stiffness



change. This requires experimental data for fracture toughness. Modification of the developed finite element approach could also be included to reduce the dependence of the results on the spatial discretization through the thickness. A methodology proposed by De Borst [21][25] using interface elements and correlating the element size to the energy released during fracture could be implemented to improved damage models. Such methodology can be used to simulate delamination in addition to matrix cracking.

## REFERENCES

- [1] Dobyns, A., Rousseau, C. Q., and Minguet, P. (2000). Helicopter Applications and Design, *Delaware Composites Design Encyclopedia*, Vol. 5, 223-242.
- [2] Cox, B., Yang, Q. (2006). In Quest of Virtual Tests for Structural Composites, *Science*. Vol.314(5802), 1102-1107
- [3] Yang, Q., and Cox, B.,(2005) Cohesive models for damage evolution in laminated composites, *International Journal of Fracture*. Vol.133,107-137..
- [4] Makeev, A., Ignatius, C., He, Y., and Shonkwiler, B. (2009). A Test Method for Assessment of Shear Properties for Thick Composites, to appear in the *Journal of Composite Materials*.
- [5] Murri, G. (1999). Influence of Ply Waviness on Fatigue Life of Tapered Composite Flexbeam Laminates, ASTM Symposium on Composite Structures: Theory and Practice, Seattle, WA
- [6] Rubin, A. M., Jerina, K. L. (1994). Evaluation of Porosity in Composite Aircraft Structures, *Mechanics of Composite Materials*, Vol. 30(6), 813-830.
- [7] Jeong H. (1997). Effects of Voids on the Mechanical Strength Ultrasonic Attenuation of Laminated Composites. *Journal of Composite Materials*, Vol. 31(3), 276-92
- [8] Peng, C., Sutton, M. A., Shreier, H. W., and McNeill, S. R. (2002). Full-Field Speckle Pattern Image Correlation with B-Spline Deformation Function, *Proceedings of the Society for Experimental Mechanics*, Vol. 49, 344-352.
- [9] [www.correlatedsolutions.com](http://www.correlatedsolutions.com), March 2009.
- [10] Camanho, P. P. and Lambert, M. (2006). A Design Methodology for Mechanically Fastened Joints in Laminated Composite Materials, *Composites Science and Technology*, Vol. 66(15), 3004-3020.
- [11] Lekhnitskii, S. G. (1981). *Theory of Elasticity of an Anisotropic Body*, Mir Publishers, Moscow.
- [12] American Society for Testing and Materials (2006). Standard Test Method for Tensile Properties of Polymer Matrix Composite Materials, ASTM Standard D 3039/D 3039M, ASTM International.
- [13] American Society for Testing and Materials (2001). Standard Test Method for In-Plane Shear Response of Polymer Matrix Composite Materials by Tensile Test of a +45° Laminate, ASTM Standard D 3518/D 3518M, ASTM International.
- [14] American Society for Testing and Materials (2005). Standard Test Method for Shear Properties of Composite Materials by the V-Notched Beam Method, ASTM Standard D 5379/D 5379M, ASTM International.

- [15] American Society for Testing and Materials (2006). Standard Test Method for Short-Beam Strength of Polymer Matrix Composite Materials and Their Laminates, ASTM Standard D 2344/D 2344M, ASTM International.
- [16] ABAQUS v6.8 Documentation, Abaqus User Subroutines Reference Manual, Section 1.1.
- [17] Echaabi, J., Trochu, F., Gauvin, R., (1996). Review of Failure Criteria of Fibrous Composite Materials, *Polymer Composites*, Vol. 17(6). 786-798.
- [18] Mar, J. W., Lin, K. Y., (1977). Fracture Mechanics Correlation for Tensile Failure of Filamentary Composites with Holes. *Journal of Aircraft*, Vol. 14(7), 703-704.
- [19] Almeida, S. F. M., Nogueira Neto, Z. S.,(1994). Effect of void content on the strength of composite laminates, *Composite Structures*. Vol. 28(2). 139-148.
- [20] Costa, M. L., Almeida, S. F. M., Rezende, M. C., (2001). The Influence of Porosity on the Interlaminar Shear Strength of Carbon/epoxy and Carbon/bismaleimide Fabric Laminates. *Composites Science and Technology*. Vol. 61, 2101-2108.
- [21] De Borst, R., (2001). Some Recent Issues in Computational Failure Mechanics, *International Journal for Numerical Methods in Engineering*. Vol. 53, 63-95.
- [22] Camanho, P. P., Davila, C.G., Pinho, S.T., Iannucci, L., Robinson, P., (2006). Prediction of in Situ Strength and Matrix Cracking in Composites under Transverse Tension and in-plane Shear. *Composites*. Vol. 37(A), 165-176.
- [23] Hahn, H.T., (1983). A Mixed Mode Fracture Criterion for Composite Materials. *Composite Technology*. Vol. 5, 26-29.
- [24] Shandu, R. S.,(1976) Nonlinear Behavior of Unidirectional and Angle Ply Laminates. *Journal of Aircraft*. Vol. 13(2), 104-111.
- [25] De Borst, R., Remmers J. J. C.,(2006). Computational modelling of delamination. *Composite Science and Technology*. Vol. 66, 713-722.
- [26] Chengye, Fan, Ben Jar, P.-Y., Roger Cheng, J.J., Cohesive zone with continuum damage properties for simulation of delamination development in fiber composites and failure of adhesive joints, *Engineering Fracture Mechanics*, Vol. 75(2008), 3866-3880
- [27] Camanho, P.P., and Davila, C.G., "Mixed-Mode Decohesion Finite Elements for the Simulation of Delamination in Composite Materials", NASA TM-2002-211737, pp. 1-37, 2002